2019

Analysis of Residual Stress and Damage Mechanisms of Thermal Barrier Coatings Deposited via PS-PVD and EB-PVD

Linda Rossmann
University of Central Florida

ANALYSIS OF RESIDUAL STRESS AND DAMAGE MECHANISMS OF THERMAL BARRIER COATINGS DEPOSITED VIA PS-PVD AND EB-PVD

by

LIN ROSSMANN
B.S. University of Central Florida, 2017
B.F.A. University of Florida, 2012

A thesis submitted in partial fulfilment of the requirements
for the degree of Master of Science
in the Department of Materials Science and Engineering
in the College of Engineering and Computer Science
at the University of Central Florida
Orlando, Florida

Summer Term
2019

Major Professor: Seetha Raghavan

ABSTRACT

Thermal barrier coatings (TBCs) are critical to gas turbine engines, as they protect the components in the hot section from the extreme temperatures of operation. The current industry standard method of applying TBCs for turbine blades in jet engines is electron-beam physical vapor deposition (EB-PVD), which results in a columnar structure that is valued for its high degree of strain tolerance. An emerging deposition method is plasma-spray physical vapor deposition (PS-PVD), capable of producing a variety of customizable microstructures as well as non-line-of-sight deposition, which allows more complex geometries to be coated, or even multiple parts at once. The pseudo-columnar microstructure that can be produced with PS-PVD is a possible alternative to EB-PVD. However, before PS-PVD can be used to its full potential, its mechanical properties and behavior must be understood. This work contributes to this understanding by characterizing PS-PVD TBCs that have been thermally cycled to simulate multiple lifetimes (0, 300, and 600 thermal cycles). Residual stress in the thermally grown oxide (TGO) layer is characterized by photoluminescence piezospectroscopy as TGO residual stress is correlated with the lifetime of the coating. Residual stress in the top coat is characterized by Raman spectroscopy, because this stress drives cracking in the top coat that can lead to failure. Scanning electron microscopy (SEM) and energy dispersive X-ray spectroscopy (EDS) are performed to observe microstructural and phase evolution to provide context and possible explanations for the stress results. In addition, EB-PVD samples of the same thermal cycling history are characterized in the same way so that PS-PVD can be benchmarked against the industry standard. The compressive residual stress in the TGO in both coatings was relieved with thermal cycling due to the TGO lengthening as well as microcracking. The PS-PVD samples had slightly lower TGO stress than the EB-PVD, which is attributed to the greater extent of cracking within the TGO, whereas cracking in the EB-PVD samples was at the TGO/topcoat interface. The PS-PVD cycled samples had significant cracking within the topcoat

near the TGO due to both greater porosity than EB-PVD samples and regions of unmelted particles that provide little resistance to cracking. The greater convolution of the TGO in the PS-PVD samples results in greater out-of-plane tensile stresses that cause crack initiation, as well as diverts cracks away from the difficult-to-follow interface. The TGO stress results agree with existing literature and extend the thermal cycling beyond what has previously been reported for PS-PVD coatings, revealing a trend of stress relief and stress values similar to that of EB-PVD coatings in this study and in the literature. Residual stress in the topcoat for both coating types became increasingly compressive with thermal cycling, indicating loss of strain tolerance by sintering. The trend of the YSZ stress for both coating types to become more compressive with cycling and with depth agrees with the literature, and the thermal cycling is longer than has been previously reported for PS-PVD. The two coating types had quite different microstructures and crack modes as well as different as-deposited residual stresses, but after thermal cycling had similar stresses in both the TGO and top coat. No samples experienced spallation. These results indicate that, while PS-PVD coatings have different properties and behavior from EB-PVD coatings, they had comparable levels of damage to EB-PVD coatings of the same lifetime and are a viable alternative to EB-PVD. Further tuning of the processing parameters may result in PS-PVD coatings with even more similar behavior to EB-PVD coatings.

"If you can achieve all of your goals, you aren't being ambitious enough." – Dr. Seetha Raghavan

ACKNOWLEDGMENTS

Heartfelt thanks to my advisor, Dr. Seetha Raghavan, for her guidance and encouragement. Thank you to Dr. Marion Bartsch, Dr. Uwe Schulz, and Dr. Ravisankar Naraparaju for helpful discussions and advice. Special thanks to Dr. Bartsch and the German Aerospace Center (DLR) for hosting me for my final three semesters. Thank you to my collaborators: Dr. Bryan Harder (NASA), Dr. Vaishak Viswanathan (Praxair Surface Technologies), and Liudmila Chernova (DLR). Thank you to Dr. Laurene Tetard for the use of her Raman spectroscopy system. Thank you to my fellow student researchers: Matthew Northam, Brooke Sarley, Chance Barrett, Johnathan Hernandez, Khanh Vo, and Ryan Hoover.

This material is based on work supported by National Science Foundation grant OISE 1460045, the Florida Space Grant Consortium (FSGC) Masters Fellowship, the FSGC Florida Space Research Program, and the Fulbright Academic Grant. This material used resources of the Advanced Photon Source, a U.S. Department of Energy (DOE) Office of Science User Facility operated for the DOE Office of Science by Argonne National Laboratory under Contract No. DE-AC02-06CH11357.

TABLE OF CONTENTS

LIST OF FIGURES

LIST OF TABLES

CHAPTER 1: INTRODUCTION

Thermal barrier coatings (TBCs) play an important role in the aerospace and power generation industries, protecting metallic engine components in the hot section of gas turbine engines from extreme operating temperatures exceeding 1200 °C [3–9]. TBCs were successfully tested in the 1970s, and were used in commercial service by the early 1980s [10]. With the use of TBCs, substrate temperatures are lower and so the coated components have greater durability and longer lifetime; they also enable the use of higher gas temperatures, resulting in greater efficiency [4, 11]. A zirconia top coat of 250 μm thickness can reduce the temperature of the substrate surface by as much as 300 °C, indicating the critical role that these coatings play in improving efficiency and performance [4].

Background: Deposition Methods for Thermal Barrier Coatings

The two industry standard methods for TBC top-coat deposition are air plasma spray (APS) and electron-beam physical vapor deposition (EB-PVD) [8, 12–14]. EB-PVD is more commonly used in aircraft jet engines, while APS is typically used for land-based power generation turbines [4, 15, 16]. Plasma-spray physical vapor deposition is a newer method that bridges the gap between the two [7, 16–18], developed out of the low pressure plasma spray (LPPS) process and intended to combine the advantages of plasma spraying with the columnar microstructure of EB-PVD [16, 17]. The development of PS-PVD began in the 1990s [19], and its refinement, optimization, and characterization continues today [20–23]. LPPS has been used to deposit alumina coatings with high wear resistance and dielectric strength for various applications, such as in the bearing industry and automotive industry [24], as well as metal coatings for engine parts and medical implants [19]; while it has been used for application of TBC bond coats, it has not been commonly used for TBC

topcoat deposition [25]. Other emerging deposition methods for TBC topcoats are suspension plasma spray (SPS), in which fine particles in an aqueous suspension are injected into the plasma and can create nanostructured coatings [26, 27], and solution precursor plasma spray (SPPS), in which an aqueous precursor is injected into the plasma jet and undergoes physical and chemical reactions before deposition, resulting in a unique microstructure with high durability [26, 28, 29].

Air Plasma Spray

In the air plasma spray (APS) process, a powder feedstock is injected into a plasma plume, where it is melted and carried to the substrate at high speed. The coating is built up as the molten droplets impinge on the substrate and rapidly solidify [7, 16].

APS coatings are typically 300 μm thick, though they can be as thick as 600 μm [4]. The surface is rough due to the fast cooling rate and the high speed at which the particles are deposited [6]. The resulting microstructure is "splat-like", with splats 1–5 μm thick and 200–400 μm in diameter, and a high degree of porosity (15–20 vol%). This porosity, along with inter-splat boundaries and cracks parallel to the layer interface, provides low thermal conductivity and a degree of strain tolerance [4, 8]. To increase strain tolerance, "dense vertically cracked" APS coatings were developed, and these coatings also exhibit greater erosion durability due to the increased density [8]. However, cracks parallel to the interface and the interface roughness reduce the coating lifetime for shorter thermal cycles. This limits the use of APS to power generation turbines, which have lower operating temperatures and temperature gradients and longer, fewer thermal cycles, and aircraft engine components subjected to less extreme conditions [4]. Nevertheless, the low production cost and fast rate of deposition of APS makes it the preferred deposition technique for its appropriate applications [4].

Electron-Beam Physical Vapor Deposition

The electron-beam physical vapor deposition (EB-PVD) method produces a more strain tolerant coating, and is the preferred deposition method for the most demanding applications [4, 8, 12]. An electron beam vaporizes a solid ingot of feedstock material, and the material condenses out of the vapor phase onto the substrate in a high-vacuum environment ($< 10^{-4}$ Torr) [7, 30]. Because the coating vapor is transported to the substrate by diffusion, the growth rate is very low [31].

The columnar structure that results has a high degree of strain tolerance, making it preferred for applications with more frequent cycling, such as aircraft engines. EB-PVD coatings also have a smoother surface, do not clog small cooling holes during deposition, and usually have a longer cyclic lifetime than APS coatings; they also have an order of magnitude improvement of erosion durability compared to APS [10, 12, 32, 33] EB-PVD coatings are also thinner than APS coatings (about 125 μm versus 300 to 600 μm for APS [4]), and therefore represent weight savings on aircraft engines.).

Plasma-Spray Physical Vapor Deposition

Plasma-spray physical vapor deposition (PS-PVD) is a process intended to bridge the gap between APS and EB-PVD, combining the cost efficiency and high deposition rate of the former with the columnar microstructure and high strain tolerance of the latter [12, 17, 18], as well as enabling customizable microstructures and the coating of more complex geometries [7, 31, 34]. Also known as very low pressure plasma spray (VLPPS) or low pressure plasma spray-thin film (LPPS-TF), PS-PVD was developed by modifying the low pressure plasma spray (LPPS) process to use higher power and much lower chamber pressure than is customary [17, 19, 20, 22]. The original work in modifying the LPPS process in this way was done at Sulzer Metco in the mid-1990s, with a

relevant patent issued in 1998, and continues to be developed by Sulzer Metco and others [19].

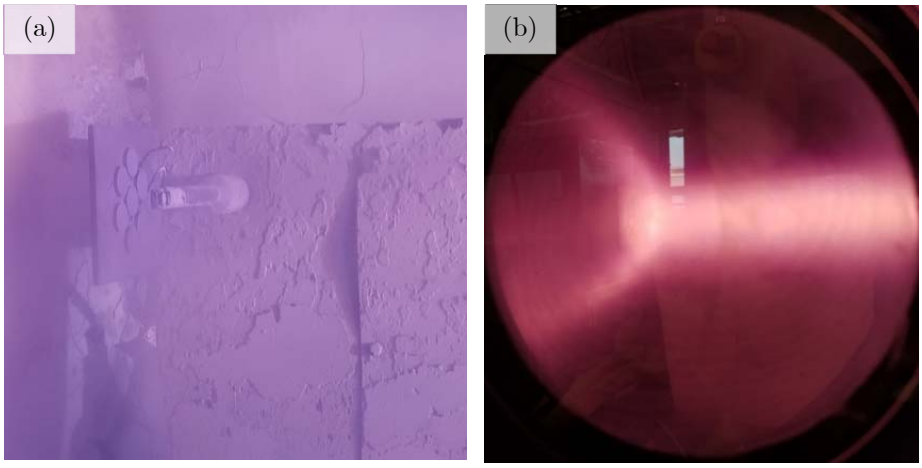

Figure 1.1: (a) Substrates from this study welded to a mounting plate inside the PS-PVD coating chamber at NASA Glenn Research Center, prior to deposition. (b) Plasma plume impinging on the substrates during deposition.

PS-PVD is done in a low-pressure environment (0.5–10 Torr), which increases the size of the plasma plume. The plasma can be over 7 feet long and 3 feet in diameter, producing supersonic gas streams ($\sim$2000–4000 m/s) and extreme temperatures (6000–10,000 K) in the core of the plasma plume [7, 16, 31]. The large size of the plasma plume enables a large area to be coated [35]. The temperature and particle velocity has a more uniform distribution than conventional plasma spray processes, and by varying process parameters, the feedstock powder can be either melted (as in APS) or vaporized (as in EB-PVD), and the microstructure can be tailored. At high feed rates a splat-like microstructure similar to APS can be produced, while low feed rates and high power produces a pseudo-columnar microstructure similar to EB-PVD [7, 31, 33]. Some non-line-of-sight coating is possible due to the evaporated material being carried by the gas stream, which is not possible with either APS or EB-PVD, and therefore allows coating of more complex geometries with shadowed areas, or even coating multiple air foils at once [7, 18, 21, 31, 35].

The attractive qualities of PS-PVD include: flexibility of resulting microstructure, coating of more complex geometries due to non-line-of-sight coverage, high rate of deposition, and lower cost than EB-PVD [7]. It is also capable of producing unique microstructures not achievable by either APS or EB-PVD [17]. In addition to TBCs, PS-PVD has the potential to be used for other applications, such as wear- or electrically-resistant coatings, environmental barrier coatings, gas-sensing membranes, diffusion barrier layers, or ion-transport layers in fuel cells [7].

Photographs of samples from this study being coated by PS-PVD at NASA Glenn Research Center are shown in Figure 1.1 and SEM micrographs comparing the microstructures of the 300-cycle EB-PVD and PS-PVD samples manufactured for this study are shown in Figure 1.2.

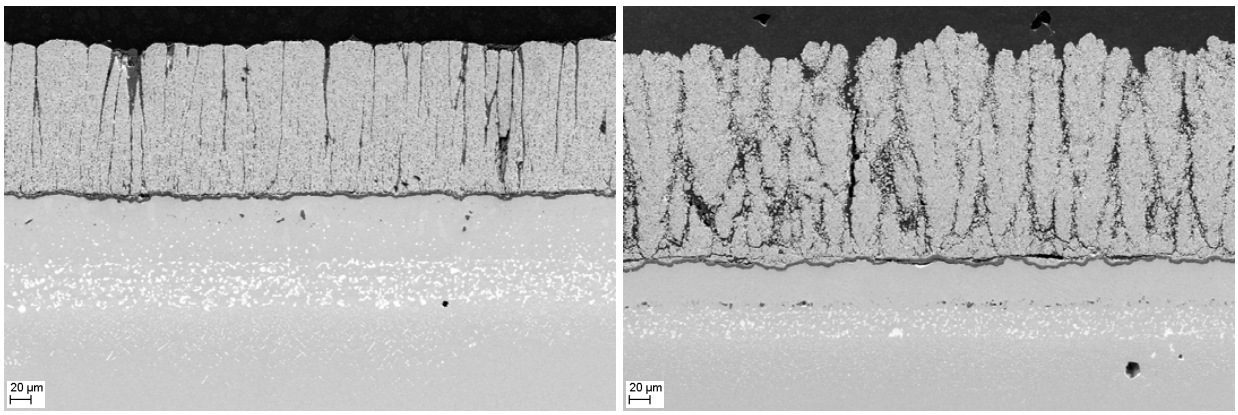

Figure 1.2: SEM cross-section micrographs of an EB-PVD sample (left) and a PS-PVD sample (right) from this study, both thermally cycled for 300 hours in air at NASA Glenn Research Center.

Background: Anatomy of an EB-PVD TBC System

A TBC system typically consists of four layers: a nickel-based superalloy substrate, a metallic bond coat layer, a ceramic top coat (usually 6–8 wt% YSZ), and a thin thermally grown oxide (TGO) layer that forms between the bond coat and top coat [4, 5, 28]. These layers are labeled in

Figure 1.3 [36]. This discussion focuses on TBCs made by EB-PVD, the industry standard for jet turbine engine blades and vanes.

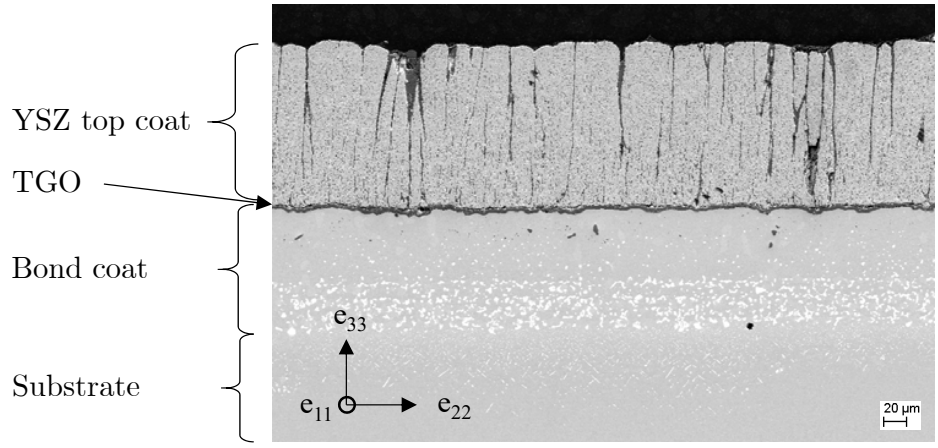

Figure 1.3: SEM cross-section image of an EB-PVD thermal barrier coating from this study with the layers labeled.

The substrate representing the turbine blade may be polycrystalline or single-crystal, and is cooled through internal channels, causing a thermal gradient from its external surface to its internal channels. The superalloy may contain many elements to improve various properties, such as aluminum to increase oxidation resistance and refractory metals to improve creep strength [37]. These alloying elements can, at operating temperatures, diffuse into the bond coat and sometimes into the TGO and top coat, where they interact with these other layers to change the properties of the TBC system over time [4, 38].

The top coat, made of 6–8% yttria-stabilized zirconia (YSZ), is the TBC component that provides thermal insulation. YSZ has one of the lowest thermal conductivities at high temperatures of ceramics, $\sim$2.3 $W \cdot m^{-1} \cdot K^{-1}$ for fully dense YSZ at 1000 °C [39], due to its high concentration of oxygen vacancies and substitutional solute atoms, which effectively scatter phonons [4]. With a columnar microstructure and multiscale porosity, the thermal conductivity can be as low as 0.5

$W \cdot m^{-1} \cdot K^{-1}$ [11]. Its high coefficient of thermal expansion (CTE), $\sim 11 \times 10^{-6} \, ^{\circ}C^{-1}$, is the closest to that of the metallic layers underneath than any other ceramic, important for reducing stresses from thermal expansion mismatch between the ceramic and metal [4]. Other important properties of YSZ include its low density, high hardness, very high melting point, and resistance to hot and ambient corrosion [4].

YSZ has five crystallographic phases: metastable tetragonal t' in as-deposited coatings, yttria-poor tetragonal t, yttria-rich tetragonal t'', yttria-rich cubic c, and monoclinic m [40, 41]. The t' phase is preferred, due to its high bending strength, high fracture toughness, high crack propagation energy, and high tolerance for thermal shock [32]. The transformation of tetragonal to undesirable monoclinic phase upon cooling is accompanied by a volume expansion of 3–5%, which places additional stresses in the zirconia and contributes to spallation failure of the TBC. Yttria (Y_2O_3) stabilizes the cubic phase while repressing the monoclinic, and a sufficiently high cooling rate also suppresses the transformation to monoclinic [32, 40–42].

The bond coat is a metallic layer 75 to 150 μm thick, which protects the substrate from oxidation and bonds the top coat to the substrate [4, 25, 30, 43]. There are two main categories of bond coat: MCrAlY alloys, and platinum and nickel aluminides [4, 6, 43]. The bond coat oxidizes at operating temperatures, as the YSZ top coat is "oxygen transparent" due to both its porosity and the high ionic diffusivity of oxygen in zirconia. This oxidation results in the TGO formation between the bond coat and top coat. The bond coat has a profound effect on the properties of the TGO, and is designed such that the TGO grows slowly and uniformly and consists of α-alumina [4, 44]. This layer serves as a barrier against further oxidation of the bond coat, due to the low ionic oxygen diffusivity in α-alumina [4]. The bond coat is of critical importance, as its composition and microstructure determines that of the developing TGO [11, 30].

The TGO is a critical factor in determining the life of the coating; EB-PVD coatings typically fail

by spallation at or near the TGO/bond coat interface [30, 45]. At high temperatures it is assumed to be stress-free, while at room temperature it experiences large compressive stresses (2–6 GPa) from the thermal expansion mismatch between it and the metallic bond coat. It also develops compressive growth stresses (generally $<$ 1 GPa) as it thickens with time at high temperature [4, 11, 46]. In the early part of the cycling lifetime, the compressive stress increases due to growth stresses from the thickening TGO layer and sometimes from transformation of transient alumina phases to the metastable phase [45]. After this initial increase, the compressive stress remains relatively constant or slowly decreases. The alumina has fully transformed to the metastable α phase, so it no longer contributes to growth stresses [4, 11]. The TGO consists of two zones of distinct microstructure, shown in Figure 1.4. The layer closest to the YSZ is an equiaxed zone of intermixed zirconia and alumina, while the layer closest to the bond coat is fully dense alumina with a columnar microstructure [11].

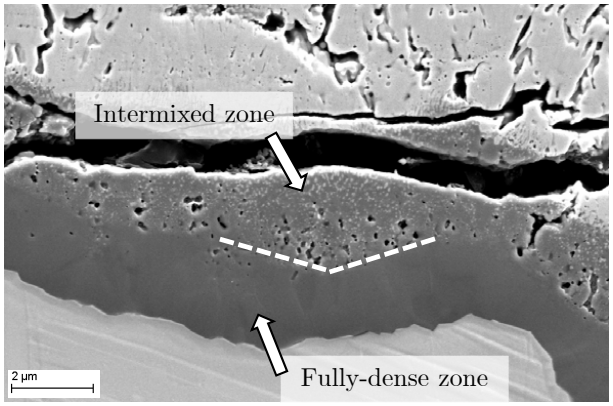

Figure 1.4: SEM cross-section image of the TGO of a thermal barrier coating from this study indicating the two distinct layers of the TGO. The dashed line marks part of the interface between the layers.

Upon cooling in a given thermal cycle, if the shear stresses in the bond coat are sufficiently greater than its yield strength, the bond coat will plastically flow from the base to the peak of existing undulations, increasing the undulation amplitudes. This process, known as “ratcheting”, occurs with

each thermal cycle when the undulation's aspect ratio (amplitude divided by wavelength) exceeds a critical value that is dependent on the TGO growth strain and the bond coat's yield strength [11]. This ratcheting allows the TGO to lengthen, which relieves some of the compressive stress in the TGO. The increasing amplitude of the undulations also results in out-of-plane tensile stresses at the crests, which allow cracks to initiate easily [4, 11]. Cracking causes local areas of increased oxidation; when enough aluminum is depleted from the underlying bond coat, other oxides may form, which reduce the oxidation-resistance of the TGO and cause additional cracking [4]. Toward the end of the TBC's life, the compressive stress decreases more rapidly due significant accumulation of damage, including cracking and delamination [45, 47]. Spallation occurs when microcracks and delaminations coalesce to allow large areas of the coating to detach by large-scale buckling; this is the most common form of failure in TBCs [4, 11]. Other phenomena that contribute to failure are sintering of the YSZ top coat at operating temperatures, which reduces strain tolerance and increases thermal conductivity, and reduction of bond strength and interfacial toughness of the bond coat by fatigue and segregation of bond coat elements and impurities, especially sulfur [4, 48].

Background: In Depth Review of PS-PVD TBCs

PS-PVD was developed to enable the rapid deposition of coatings with a customizable microstructure by its capability to melt and/or vaporize the feedstock powder, bridging the gap between EB-PVD and the thermal spray processes [7, 14, 16, 17, 49].

PS-PVD is related to the more established methods of spray coating in a controlled atmosphere, including LPPS (also called vacuum plasma spraying (VPS)) and low vacuum plasma spray (LVPS), all of which are performed in a low pressure environment, often with an argon gas atmosphere [16, 17, 25, 31, 50, 51]. The pressure ranges of these processes are typically between 50 and 200 mbar (38 to 150 Torr), and this reduced pressure decreases the atomic collision rate and therefore

enlarges the plasma plume up to 500 mm in length and 40 mm in diameter [16, 25, 51]. The larger plasma plume is advantageous in that the temperature and particle velocities are more uniform in the plume, resulting in a more consistent coating thickness [16, 17, 31, 51]. PS-PVD was first achieved by modifying an LPPS system to operate at high power and chamber pressures significantly lower than typically used for LPPS, and is sometimes called very low pressure plasma spray (VLPPS) [19]. Typical chamber pressures for PS-PVD are in the range of 0.5 to 2 mbar (0.4 to 1.5 Torr), which greatly expands the plasma plume to over 2 m long and 400 mm in diameter [16, 25]. The injected material is carried by the plume at extremely high speeds (around 2000 m/s at 1 mbar and 6000–10,000 K), which makes it possible to coat areas that are not in the line of sight, enabling more complex geometries to be coated [16, 25, 31, 51]. Non-line-of-sight coating with PS-PVD has been demonstrated [34], including a double vane dummy that was successfully coated with a pseudo-columnar microstructure, even in shadowed regions, and a thickness distribution similar to that of a single blade coated alone [31].

In addition to liquid and vapor phase deposition, there can also be a hybrid situation in which nano-sized clusters are first deposited [12, 25]. As deposition continues, some crystal orientations grow faster than others and become columns. The slower-growing columns stop growing when they are close to another column, and the remaining gaps between the crystals create porosity that increases strain tolerance [12, 25].

Growth at the beginning of deposition is three-dimensional island growth, with vapor atoms and nanoclusters condensing to form the islands. These islands grow and join up with each other in a manner similar to EB-PVD [51]. Later stages of growth differ from EB-PVD, because the vaporized material is carried by a supersonic gas stream. Whereas in EB-PVD the adatoms have great mobility and adsorb onto existing crystals, resulting in regular, well-arranged columns, in PS-PVD the high-velocity nanoclusters have lower mobility. These clusters can form a nucleation cluster on an existing column, making the columns less regular. The shadowing effect is also

intensified, resulting in larger, randomly oriented crystals [20, 51]. Shadowing is the result of the direction of the impinging particles with the roughness of the growing surface. Because the clusters have insufficient mobility, the roughness is enhanced rather than smoothed, producing columns that are wider at the top and have voids between them; this structure can be seen in Figure 1.5b, in contrast to the denser and more uniform columnar structure in Figure 1.5a. Shadowing may be overcome by disruption of the plasma flow farther from the jet axis, such as vortices and reverse flow [52]. When the substrate temperature is higher, surface diffusion may partially overcome the shadowing effect, and the intercolumnar gaps begin to fill and the columns have preferential growth and a more faceted shape [51, 52].

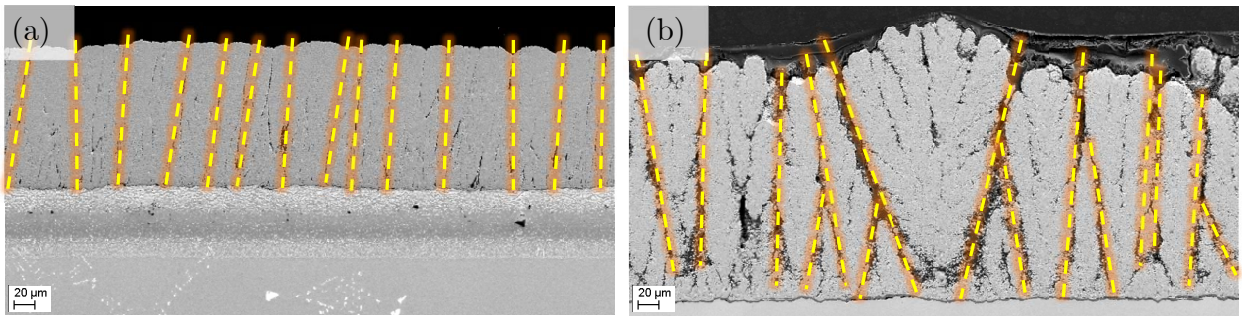

Figure 1.5: Cross-section SEM micrographs of an uncycled EB-PVD sample (a) and an uncycled PS-PVD sample (b) from this study. Dashed lines have been added to mark the column edges. The PS-PVD sample has tapered columns.

The effects of some processing parameters are discussed below.

- *Plasma gas composition* — Adding helium concentrates the plasma flow and the particle plume due to its higher viscosity relative to hydrogen, whereas adding hydrogen broadens it [17, 25]. Increased He content also increases the plasma enthalpy and raises the plasma temperature, resulting in coatings with a greater degree of vapor deposition (relative to splat-like deposition) [7, 25].

- *Plasma gas flow rate* — Higher plasma gas flow rate increases the chamber pressure [7].

- *Chamber pressure* — Lower pressure produces a more columnar microstructure, especially when combined with higher power [7]. Higher pressure also produces a denser coating; the plasma plume is smaller at high pressure, allowing the material to cool more before it reaches the substrate, resulting in slower growth that is less conducive to formation of voids during growth [7].

- *Plasma power* — Higher plasma flow rate pushes the arc farther from the torch, which increases the voltage and therefore increases the plasma power for the same amperage. Low power produces wider columns [7].

- *Plasma enthalpy* — Low enthalpy conditions can result in coatings with traces of monoclinic zirconia and yttria, possibly because the zirconia and yttria are inadequately mixed because the plasma plume is less homogeneous [7].

- *Powder feed rate* — Lower powder feed rate also increases the degree of vaporization, resulting in a pseudo-columnar microstructure [17, 33].

- *Spray distance* — A study on spray distance [53] found that greater spray distance (from 0.6 m to 1 m) decreases the amount of monoclinic phase and zirconia suboxides (ZrO_{2-x}) and increases the degree of vaporization. The greater degree of vaporization may be due to particles spending more time in the hot plasma during which they may vaporize, or due to unmolten particles falling from the plasma plume during the longer distance. Increasing the spray distance further to 1.4 m, however, resulted in re-solidified nanoparticles sticking to the columns, a sign of reduced heating capability at this distance. The coatings with a 1 m spray distance, which had the highest degree of vaporization and most columnar microstructure, also had the lowest porosity and highest hardness and Young's modulus [53].

The widths of columns in pseudo-columnar PS-PVD coatings are typically wider than EB-PVD columns, on the order of 10–40 μm compared to 5–10 μm [7, 33, 53]. The columns are broader

near the top of coating than near the interface and exhibit intracolumnar porosity. Intercolumnar gaps are observed, containing small particles resulting from incompletely vaporized powder; examples are marked in Figure 1.6. The surface texture is often "cauliflower-like" and the columns more cylindrical than the highly faceted EB-PVD columns, which are more highly textured [33].

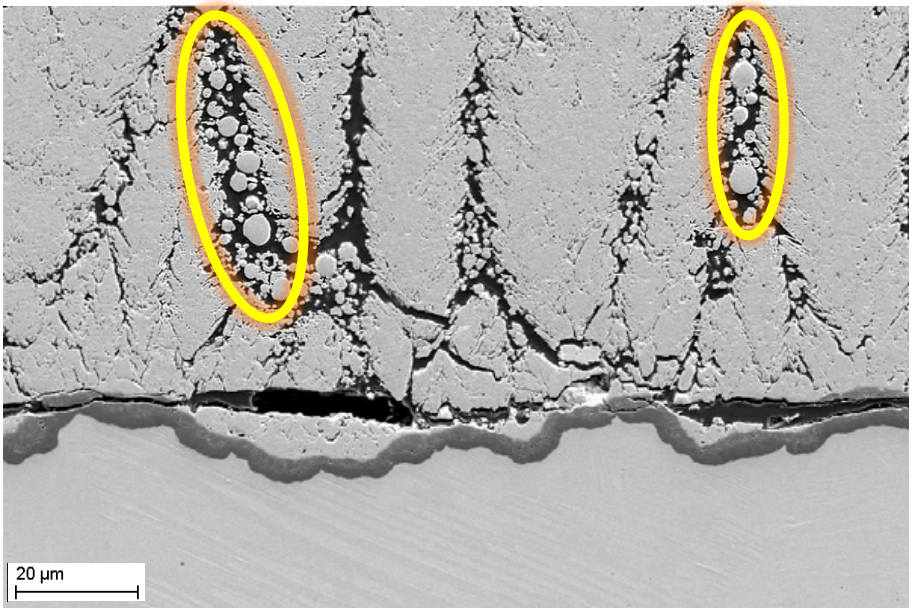

Figure 1.6: Cross-section SEM image of a PS-PVD coating from this study, with incompletely vaporized particles in the intercolumnar gaps circled.

The erosion rate of PS-PVD coatings is dependent on the processing parameters and resulting features such as widths of columns and intercolumnar gaps. Coatings with fine columns and wide gaps can have higher erosion rate than APS coatings due to low mechanical strength, while coatings optimized to reduce the intercolumnar gaps had erosion rates between APS (high erosion) and EB-PVD (low erosion) coatings [31].

Some PS-PVD coatings with both PtAl and CoNiCrAlY bond coats have out-performed EB-PVD with CoNiCrAlY in furnace cycling tests at 1135 °C, lasting up to 700 cycles with no spallation [31]. PS-PVD coatings have been found to have similar resistance to simulated sand ingression as

EB-PVD coatings [18].

Motivation

The advantages of PS-PVD, particularly customizable microstructure and ability to coat more complex geometries, make it an appealing process that opens new avenues of coating development. However, the properties and behavior of PS-PVD coatings must be understood before the process can be used to its fullest. This work characterizes PS-PVD coatings at multiple lifetimes to gain insight into its durability and damage modes. EB-PVD coatings with the same thermal cycling history are also characterized in the same way, thereby benchmarking the performance of PS-PVD coatings against the industry standard and providing insight into the extent to which it is a possible alternative to EB-PVD coatings.

The goals of this work are to evaluate PS-PVD coatings using EB-PVD coatings as a baseline with the following objectives:

- Characterize the residual stress in the TGO layer and its evolution with thermal cycling via photoluminescence piezospectroscopy. The TGO is the most common site of failure of EB-PVD coatings, which have microstructural similarities with PS-PVD coatings, and so is critical to component lifetime. Stress relief in the TGO is an indicator of damage and thus provides information on the health and lifetime of the coating. Stress maps will be made at multiple lifetimes, showing the evolution of the average stress as well as the spatial distribution of stresses.

- Characterize the residual stress in the YSZ top coat, its distribution with depth, and its evolution with thermal cycling via Raman spectroscopy. The region of the top coat near the TGO interface is the most common failure site in APS coatings, with which PS-PVD coatings

also have similarities. As residual stress in the YSZ drives cracking which leads to failure, understanding the evolution of this stress is important for evaluating the lifetime of the coating. Stress measurements averaged over a wide sample area will be made at multiple depth positions in each sample for samples at multiple lifetimes, showing the distribution of stress with depth and its evolution.

- Characterize the microstructure and damage modes at multiple lifetimes via scanning electron microscopy of coating cross-sections. Qualitative observations of the microstructure and damage will provide context for interpretation of the spectroscopy results and will support the stress results.

Overview of Research

Thermal barrier coatings are critical to the aerospace and power generation industries for protecting components in the hot sections of gas turbine engines. The two industry-standard methods of deposition, APS and EB-PVD, each have their advantages and drawbacks. A newer method, PS-PVD, bridges the gap between the two, combining the low cost and high coating rate of APS with the superior coating quality of EB-PVD; it also offers additional advantages such as the ability to coat complex shapes and even multiple parts at once. However, before the PS-PVD method can be adopted commercially, its microstructure, properties, and behavior under operating conditions must be understood.

To that end, this work compares TBC samples made by PS-PVD and EB-PVD in their new, uncycled condition, and after multiple amounts of thermal cycling. Investigations are made with non-destructive spectroscopy methods, as well as optical and scanning electron microscopy. Chapter 1 has provided the motivation of the work and background information on the TBC deposition methods. Chapter 2 provides the details on the sample manufacturing and thermal cycling. Chapter 3

gives information on the characterization techniques used, the data collection procedures, and the data analysis procedures. The spectroscopy findings are given in Chapter 4, and the microscopy findings in Chapter 5. Lastly, further discussion and conclusions are provided in Chapter 6.

CHAPTER 2: SAMPLE MANUFACTURING

Samples were manufactured to study PS-PVD TBCs and compare them to industry-standard EB-PVD TBCs at three lifetimes — uncycled, 300 cycles, and 600 cycles. All samples had the same substrate, René N5 single-crystal nickel-based superalloy disks 25.4 mm in diameter and 3 mm thick. An industrial standard platinum aluminide (PtAl) bond coat was applied by Praxair Surface Technologies. The expected composition of the René N5 is listed in Table 2.1 [54].

Table 2.1: Typical composition of René N5.

Element	Co	Cr	Al	Ta	W	Re	Mo	Hf	Ni
wt%	8	7	6.2	6	5	3	2	0.2	bal.

All samples were coated with a top coat of 6–8 wt% yttria-stabilized zirconia with a target thickness of 200 μm. Thirty-five samples were designated for PS-PVD with seven for each intended cycling lifetime and ten to remain uncycled. These were divided into five batches of seven, the greatest number of samples that could be coated simultaneously in the PS-PVD deposition chamber at NASA's Glenn Research Center. Of the thirty-five samples manufactured, fifteen are included in this study. Nine samples were designated for EB-PVD, with three for each cycling lifetime; these were coated by Praxair in a single batch.

Details of PS-PVD Coating

For each PS-PVD coating batch, the seven bond-coated substrates were each measured in thickness with calipers, with the average of two thickness measurements used. The seven substrates

were then spot-welded to an Inconel 716 superalloy plate in a hexagonal pattern with two K-type thermocouples spot-welded between them; this arrangement is shown in Figure 2.1.

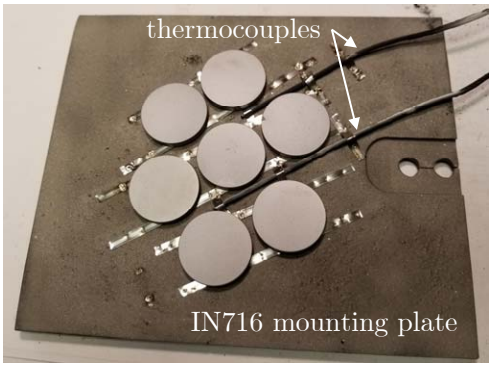

Figure 2.1: Bond-coated samples spot-welded to a mounting plate prior to PS-PVD coating.

The mounting plate was clamped to a bracket inside the coating chamber, which was then pumped to a vacuum under 0.2 Torr and left for several hours to reduce humidity in the chamber. Then the chamber was back-filled with argon to 30 Torr and the plasma torch was lit, using an argon-helium gas mixture. The chamber was pumped down to about 1 Torr. The plasma plume impinged on the mounted samples and preheated the samples to approximately 750 °C before the powder was injected. The yttria and zirconia powders were then injected into the plume by two feeders and continued for about 30 minutes. During coating, the temperature readings from the two thermocouples were monitored and recorded.

Table 2.2: Processing parameters for PS-PVD.

Substrate temp.	Current	Power	Pressure	Spray distance	Ar/He ratio	Total plasma gas
800–850 °C	1800 A	80 kW	0.785 Torr	1.65 m	1:2	80 NLPM

After each coating run, the samples' thicknesses were measured as before and compared to the

pre-coating thicknesses to determine the coating thickness. The resulting thickness information was used to adjust the coating time for the subsequent coating batch to more accurately achieve the target thickness; times between 26 and 30 minutes were used for the five coating runs. Table 2.2 lists the process variables. These values had been previously tuned to produce pseudo-columnar coatings similar to those produced by EB-PVD [7, 14, 33].

The target thickness for each sample's top coat was 200 μm to be comparable to industry-standard EB-PVD coatings. The PS-PVD samples had a mean thickness of 217.6 μm and a standard deviation of 35 μm. The EB-PVD samples had a mean thickness of 218.6 μm and a standard deviation of 26 μm. Thicknesses were measured with calipers and the average of two measurements was used. Because the EB-PVD samples were not measured for thickness between bond coat and top coat deposition, these thicknesses were calculated from the substrate thickness plus the average bond coat thickness, which was determined using the PS-PVD samples.

Cyclic Thermal Aging and Sample Slicing

The PS-PVD samples are oxygen-deficient in their as-coated state due to the low partial pressure of oxygen during deposition; this can be seen in their dark gray to black color, evident in Figure 2.2a. The samples were given a heat treatment to convert the as-deposited ZrO to the desired ZrO_2, after which the coatings appear white, as seen in Figure 2.2b. The temperature in the oven was increased from room temperature to 1100 °C at a rate of 5 °C per minute, held at 1100 °C for one hour, and then ramped down at 5 °C per minute. This heat treatment also served to develop a TGO in the samples. The average roughness of the PS-PVD samples after the heat treatment was 9.3 $\pm$ 0.6 μm Ra, while the average roughness of the as-deposited EB-PVD samples was 2.1 $\pm$ 0.4 μm Ra as measured by optical profilometry (Zygo NewView 7200 profilometer).

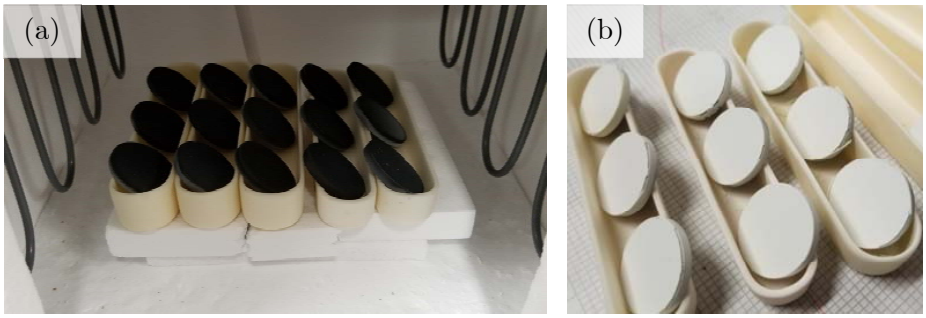

Figure 2.2: As-deposited PS-PVD samples in a furnace prior to heat treatment (a), and PS-PVD samples after heat treatment (b).

Three of the nine EB-PVD samples did not receive any thermal cycling, and are designated as the "uncycled" samples. Two samples from each of the five PS-PVD batches did not receive any additional thermal cycling, reserved for comparison to the uncycled EB-PVD samples. The five batches were divided among five cycling times. The numbers of samples per thermal cycling history considered in this work are listed in Table 2.3.

Table 2.3: Number of samples per coating type and thermal cycling.

	Uncycled	300 Thermal Cycles	600 Thermal Cycles
EB-PVD	2	3	3
PS-PVD	7	4	4

Thermal cycling was done in an open-air furnace with a hot temperature of 1100 °C, monitored by a K-type thermocouple. Each cycle had a hot time of 1 h and a cool time of 10 min. During the cool time, cooling was assisted with a fan and the temperature reached 200 °C.

After thermal cycling, pseudo-rectangles of approximately 2.5 mm width were cut from the discs' centers using a diamond saw, as shown in Figure 2.3. The samples were then rinsed with cold water

and dried with compressed air. The width was chosen to be narrow enough for transmission X-ray diffraction (XRD) measurements through the cross-section, while being wide enough to minimize edge effects [55]. Initial XRD results have been published in our other work [56].

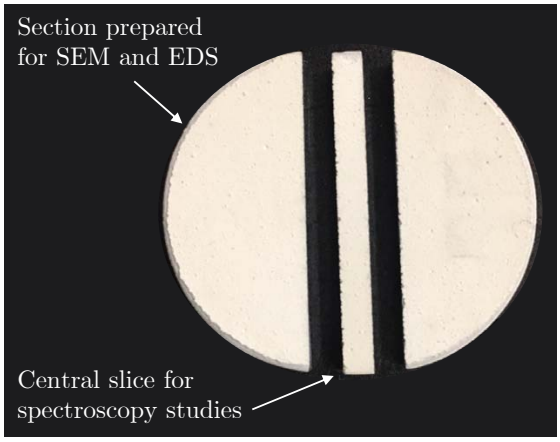

Figure 2.3: Central pseudo-rectangular slice cut from a disc sample.

Metallographic Preparation and Microscopy

While the 2.5 mm-width specimens taken from the center of each disk were used for spectroscopic studies, other pieces of the samples were used for microscopy studies of the microstructure. For each sample used for microscopy, one piece was encased in cold-set two-part epoxy and allowed to cure for 24 hours. A slice from the center of each piece was cut on a diamond wire saw using water-free silicone oil as the cooling fluid, to avoid risk of moisture-induced spallation. Each slice was embedded in conductive carbon material and polished, the final polishing step using 0.04 μm colloidal silica, and then ion-beam etched using a Gatan High Resolution Ionbeam Coater Model 683 with auxilliary etching equipment. Sample slices were then imaged with a ZEISS ULTRA55 scanning electron microscope (Zeiss SMT, Oberkochen, Germany) equipped with a field emission gun.

CHAPTER 3: METHODS OF CHARACTERIZING STRESS AND DAMAGE IN TBCS

The primary characterization methods used in this work are the non-destructive, non-contact methods of Raman and photoluminescence (PL) piezospectroscopy. PL spectroscopy is used to investigate the residual stress evolution in the thermally grown oxide layer, which is critical to spallation lifetime. Raman spectroscopy is used to investigate the stress evolution in the the YSZ top coat. Scanning electron microscopy (SEM) is used to support observations from the spectroscopy data, such as cracking and delamination responsible for stress relief, as well as to provide information to identify the responsible phenomena. Energy dispersive X-ray spectroscopy (EDS) is used in conjunction with SEM to provide elemental composition information and identify phases.

Raman Spectroscopy for Phase Identification and Stress Measurements in YSZ Topcoats

Raman spectroscopy makes use of the inelastic scattering of incident monochromatic light. When laser light of frequency ν_0 interacts with a sample, it is scattered. Most of the light is elastically scattered, with the scattered light having the same frequency ν_0 as the incident light, called Rayleigh scattering. However, for molecules with Raman-active modes, the electromagnetic oscillation of the incident light interacts with the molecular vibrations, resulting in inelastic Raman scattering. The Raman scattered light has frequency $\nu_0 \pm \nu_m$, where ν_m is a characteristic frequency arising from the particular molecular vibration and phonons in the material. The frequencies of the characteristic Raman peaks provide information on the composition of the material, and shifts in a characteristic peak's frequency provide information on the strain in the material [57–59]. When investigating YSZ, it should be noted that Raman spectroscopy does not easily distinguish between the tetragonal (*t*) and tetragonal prime (*t'*) phases; the same six characteristic peaks ap-

pear for both phases, with the peaks becoming more narrow as the (*t*) content increases [60, 61]. For this reason, peaks identified as (*t*) in this study should be understood to be the sum of these two phases. Raman spectroscopy is highly sensitive to the monoclinic zirconia phase, which has 4 molecules per unit cell and 18 Raman active vibration modes, and has low sensitivity to the cubic phase, which has one molecule per unit cell and only one Raman active mode. It is moderately sensitive to the tetragonal/tetragonal prime phase, which has two molecules per unit cell and six Raman active modes [62]. The Raman shifts of YSZ measure the mean strain, $\varepsilon_{11} + \varepsilon_{22} + \varepsilon_{33}$ [61].

Previous Raman Investigations of TBCs

Raman spectroscopy has been used to study the evolution of the residual stress in the YSZ topcoat of TBCs and offers advantages such as very high spatial resolution (on the order of several μms) and potentially large penetration depth [63–65]; the high spatial resolution enables measurement of individual YSZ columns [66]. Residual stress in as-deposited EB-PVD coatings has been found to be highly dependent on deposition conditions [64] and is more compressive closer to the interface with the metallic bond coat [64, 65]. The distribution of stress has been found to be approximately linear in some studies [64], while others have reported constant stress in the bulk of the coating with reduced compressive stress near the surface [66]. Raman stress measurements have been made both nondestructively, with the incident laser perpendicular to the coating surface [22, 66], as well as on polished cross-sections [64, 65]. Raman spectroscopy has been performed on a freestanding APS coating to produce a stress map 60 $\times$ 60 μm with a point spacing of 4 μm, with the resulting features of the stress map corresponding to pores and local crystal structure [67]. It has also been used to study the effect of sand ingression on residual stress through coating depth [65]. Raman stress measurements on thermally cycled PS-PVD samples have shown that the as-deposited topcoat stress is tensile and becomes compressive after about 100 thermal cycles, then becomes increasingly compressive with further cycling up to 300 cycles [22].

Raman spectroscopy is a preferred technique for measuring the evolution of the monoclinic zirconia phase due to its high sensivitiy to that phase [23, 60]. The first appearance of the monoclinic Raman peaks after various thermal treatments has been used to study the transformation kinetics of YSZ [60], and distribution of monoclinic phase in PS-PVD coatings has been used to study deposition mechanisms [23]. Mapping of monoclinic and tetragonal phases during cooling from thermal exposure has also been achieved using Raman spectroscopy [68].

Raman Spectroscopy Procedure

A Witec UHTS-300 spectrometer with a grating of 1800 grooves/mm was used with a 20x magnification lens and a 532 nm laser at 20.24 mW power. At this magnification, the spot size diameter in the xy plane was 0.811 μm and the spot depth range was 6.650 μm, for a probed volume per measurement point of 3.463 μm^3. The measurement center wavelength was 543.567 nm, and the spectral center was 399.999 relative cm^{-1}. At each measurement location, a 3 $\times$ 3 grid of measurements were taken, each with an area of 2 $\times$ 2 μm and a 1 s integration time, and these 9 spectra were averaged together to produce a spectrum for that 6 $\times$ 6 μm region. In some cases, measurement points further beneath the surface produced very noisy spectra; in these cases the integration time was increased to 5 s to achieve an adequate signal to noise ratio for deconvolution. For each sample, a grid of 20 points on the surface of the top coat was measured, with each point having confocal measurements at five depths into the coating (0 (surface), -50, -100, -150, and -200 μm). Points were spaced every 0.5 mm across the width of the sample from cut edge to cut edge (about 2.5 mm), and spaced every 1 mm down the length of the region of interest on the sample (parallel to the cut edges), for a total grid size of 2.5 $\times$ 4.0 mm^2. Because the instrument's automated stages do not have the range required, the stages were adjusted manually. Alignment of surface features in the microscope view with a reference line 100 μm from the edge of the field of view was used to determine the distance to move. Confocal depth measurements were spaced

50 μm apart for a total depth of 200 μm below the coating surface. Spectra from all 20 points at a given depth into the coating were averaged together, for a total of five spectra, one per depth level. This averaging was done to sample a large volume. Figure 3.1 illustrates the measurement geometry and averaging strategy.

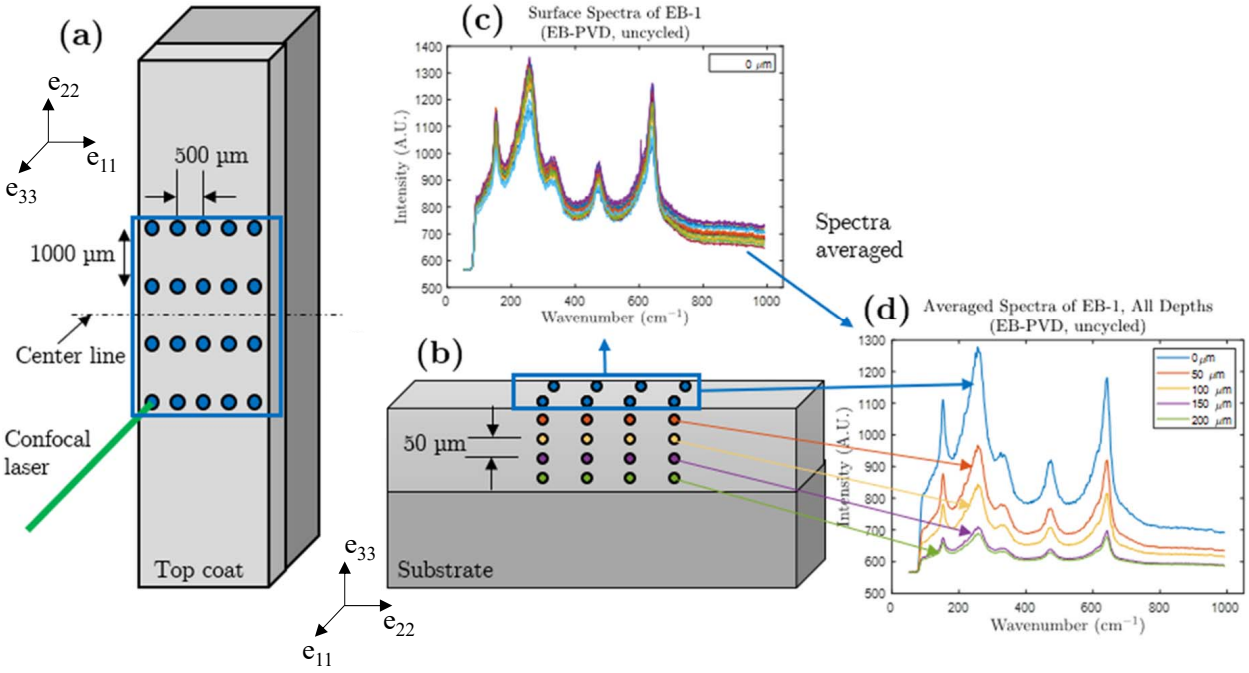

Figure 3.1: Measurements were taken in a grid of 20 points in the e_{11}–e_{22} plane (a), with each point having 5 confocal measurements in the e_{33} direction into the coating (b). The spectra from all 20 measurements at a given depth (c) were averaged together, producing 5 spectra, one for each e_{33} position (d).

Raman Analysis Procedure

A plane stress condition was assumed ($\overline{\sigma}_{33} = 0$), and it was further assumed that $\overline{\sigma}_{11} = \overline{\sigma}_{22}$ [67, 69]. Biaxial stress is related to the Raman peak shift from the unstressed reference using the

piezospectroscopic coefficient (PSC), as shown in Equation 3.1.

$$\sigma_{biaxial} = \frac{\nu - \nu_{\text{ref}}}{\text{PSC}} \tag{3.1}$$

The characteristic tetragonal peak at about 640 cm^{-1} was chosen for stress measurements due to its high intensity and its use in prior literature for PS-PVD samples. The starting powder used to make the PS-PVD coatings was used as the stress-free reference (the fitted location of the peak being 636.9 cm^{-1}, similar to that reported in literature [22]). For the PS-PVD samples, a PSC of -25 cm^{-1}/GPa was used, as in [22, 67]. The reference sample for the EB-PVD coatings was a high-purity 8YSZ powder used to make the ceramic ingots that are the feedstock for the EB-PVD process; the fitted peak position was 644.26 cm^{-1}, close to the value of 643.78 cm^{-1} reported in literature [66]. The PSC for the EB-PVD samples was -5.43 cm^{-1}/GPa, taken from literature [66]. The large difference in the PSCs is due to the very different microstructures, especially the degree of porosity [66]; the much greater porosity of PS-PVD makes it more compliant and thus have a higher PSC. It should be noted that the PSCs are sometimes reported as positive values in literature; this is because compressive stress is often reported as positive. In both this work and in the literature, shift to a higher wavenumber indicates more compressive stress.

When using the 640 cm^{-1} peak, the overlapping characteristic tetragonal peak at 610 cm^{-1} must be deconvoluted from the 640 cm^{-1} peak for accurate fitting results. Many spectra contained additional overlapping peaks that must also be deconvoluted. The fitting code first fit the spectrum region of interest with four pseudo-Voigt peaks with user-specified initial guesses, then calculated the goodness of fit (GoF) in the wavenumber range of interest by normalized root mean square error. If the GoF was below a specified threshold, a three-peak fit was done, and if that GoF was also below a threshold, a two-peak fit was done. The fit with the highest GoF was kept. An example fit with four peaks is shown in Figure 3.2.

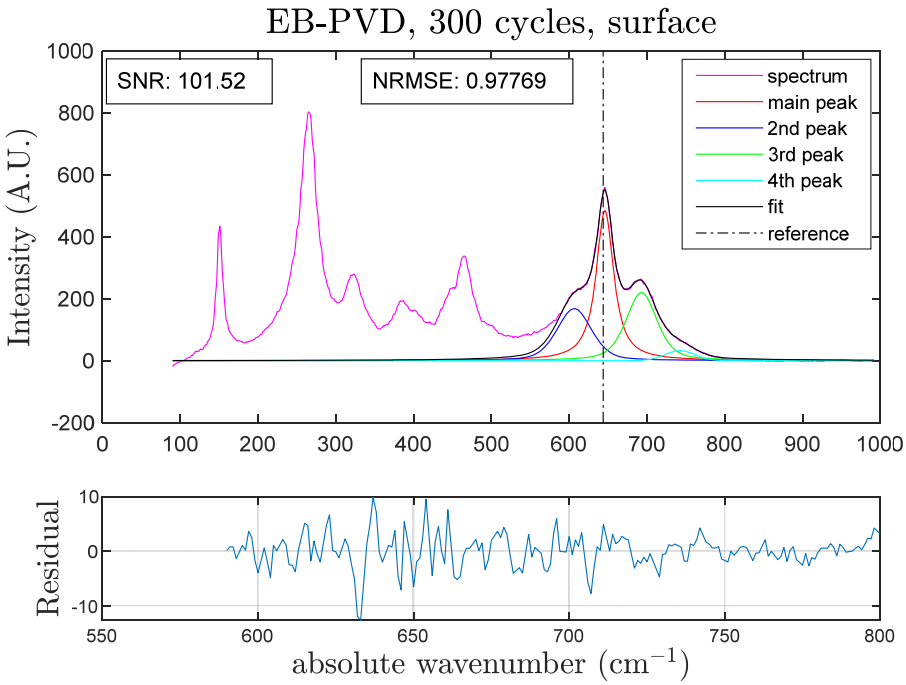

Figure 3.2: Representative Raman spectrum with peaks fit in the region of the 640 cm^{-1} peak. The subplot shows the residual of the fit.

Photoluminescence Piezospectroscopy for TGO Stress Measurements

Because the thermally grown oxide (TGO) layer consists chiefly of α-alumina, its stress state can be investigated by the photoluminescence [70]. Chromium ions (Cr^{3+}) present as trace impurities in the alumina fluoresce when optically excited, and the wavelength of the fluorescence doublet shifts systematically with applied stress, known as the piezospectroscopic effect [1], as shown in Figure 3.3 (figure made in part using VESTA [71]). This effect was first studied in ruby (Cr-doped α-alumina) [70], giving the name "R lines" to the doublet, and has been used to measure the pressure in diamond anvil cells since the early 1970s [1].

Alumina has a trigonal crystal structure, with Al ions occupying two-thirds of the octahedral interstitials between layers of oxygen. Each Al ion is surrounded by a nearly-octahedral arrangement of

six oxygen ions, with three of the oxygen ions about 5% farther from the Al than the others, reducing the point symmetry. The doped Cr^{3+} ions occupy the Al positions [70]. This asymmetry in the electrostatic crystal field causes the ^2E energy levels to split, causing a doublet consisting of two distinct R1 and R2 fluorescence lines [72]. Because the Cr^{3+} ion is substituted in a tightly-bound material with a high elastic modulus, its fluorescence lines are very sharp, and are only broadened by phonon scattering [72].

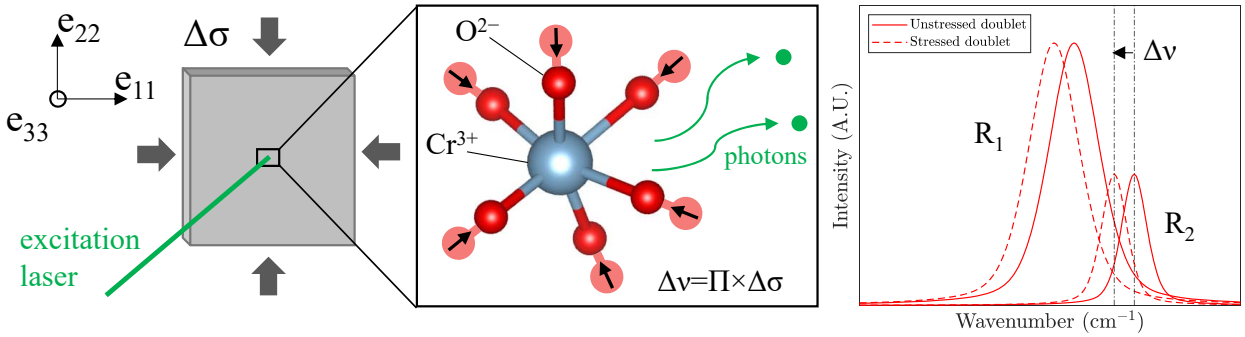

Figure 3.3: Schematic illustration of the piezospectroscopic effect in chromium-doped alumina. When stress is applied to the alumina, the lengths of the ligands change, which changes the frequency of the photons emitted during fluorescence.

The change in frequency $\Delta\nu$ of a fluorescence line can be expressed by the tensorial equation

$$\Delta\nu = \Pi_{ij}\sigma^*_{ij} \tag{3.2}$$

where Π_{ij} are the piezospectroscopic coefficients and σ^*_{ij} is the stress state defined in terms of the crystallographic lattice [1]. It is assumed that for a single isolated dopant ion, such as Cr^{3+} in alumina, the form of the piezospectroscopic tensor is determined by the point symmetry of the dopant ion in the host lattice. The frequency shift of the R lines under pure shear has been reported to be within the measurement uncertainty, and so the effects of shear stress can be neglected and

the off-diagonal PSC tensor components assumed to be zero; this is expected for crystals with rotational symmetry about the *c* axis [1].

$$\Pi_{ij} = \begin{bmatrix} \Pi_{11} & 0 & 0 \\ 0 & \Pi_{22} & 0 \\ 0 & 0 & \Pi_{33} \end{bmatrix} \tag{3.3}$$

While the frequency shift of the R1 line exhibits nonlinearity, the R2 line frequency shift has a linear dependence on the trace of the stress tensor ($\sigma_{11} + \sigma_{22} + \sigma_{33}$) and so is preferred as a measurement of mean stress [70, 73]. In the case of Cr-doped alumina, the reference frame has the 3-axis parallel to the crystallographic *c* axis, the 1-axis parallel to the *a* axis, and the 2-axis parallel to the *m* axis [1]. The piezospectroscopic coefficients for Cr-doped alumina as reported by He and Clarke [1] are listed in Table 3.1. The stress-free wavenumbers are 14402 cm^{-1} for R1 and 14432 cm^{-1} for R2 [74–76].

Table 3.1: Piezospectroscopic coefficients for Cr-doped alumina (α-alumina) [1].

	Π_{11}	Π_{22}	Π_{33}	$\Pi_{11} + \Pi_{22} + \Pi_{33}$
R1	2.56	3.50	1.53	7.59
R2	2.65	2.80	2.16	7.61

Because a thermally grown oxide is very thin (less than 6 μm [30]) and essentially planar, it is assumed to be in a biaxial stress state [77]. In this case, the frequency shift is expressed as

$$\Delta\nu = \frac{2}{3}(\Pi_{11} + \Pi_{22} + \Pi_{33})\sigma_B \tag{3.4}$$

where σ_B is biaxial stress [78]. Multiplying the values of $\Pi_{11} + \Pi_{22} + \Pi_{33}$ given in Table 3.1 by

two-thirds produces biaxial coefficients of 5.06 cm^{-1}/GPa for R1 and 5.073 cm^{-1}/GPa for R2.

Temperature and concentration of Cr^{3+} ions also affect the frequency of the R lines. When the Cr^{3+} ion concentration is greater than 0.5%, electronic interactions between the Cr^{3+} ions cause large nonlinear changes in fluorescence behavior. However, for lightly-doped polycrystalline alumina such as that in a TGO, the effect is negligible [79]. The temperature correction coefficients for both R lines are around -0.14 cm^{-1}/K, with the R1 coefficient slightly higher [70]. At 300 K a temperature uncertainty of ± 1 K is equivalent to a stress uncertainty of $\pm$ 27.6 MPa, so the effect of temperature on stress results is minimal.

When all dopant ions contributing to the fluorescence experience the same stress, the fluorescence shifts in frequency but does not change in shape or width. In this case, the spectrum can be fit with a single R1/R2 doublet. However, when the fluorescing region is in a heterogeneous stress state, the luminescence is the sum of the luminescence of each individual Cr^{3+} ion, and so the peak changes shape and becomes broader. Peak broadening has been found to be proportional to the stress variation in the fluorescing volume [78]. The area fraction of the less-stressed doublet to the total doublet area, called bimodal fraction, can be used as an indicator of local damage. The less-stressed doublet originates from regions of local cracking or delamination, where the TGO is no longer constrained [9, 45, 78, 80].

Previous PLPS Investigations of TBCs

PLPS is a nondestructive method that has been used extensively to characterize the residual stress in the TGO of TBCs [15, 22, 45, 48, 73, 78, 81, 82]; it is a direct measure of local elastic strain energy in the TGO [78], which drives cracking and spallation failure [11]. The luminescence signal is strong and can be detected through the topcoat of the TBC [83]. Data sets of PLPS measurements have been combined with statistical methods and neural networks to provide reliable predictions

of remaining lifetime [84], and measurements made at more than one point during cycling have enabled the prediction of rate of change of stress and time remaining to reach a critical stress level [85].

An advantage of the PLPS method is its ability to create contour maps showing the spatial distribution of TGO stress as well as regions of stress relief that indicate local damage. In one study, TGO stress maps measuring 4.4 $\times$ 5.6 mm with spatial resolution of 16 μm were made by PLPS at multiple lifetimes; the stress variation was fit to a Gaussian distribution and it was concluded that the measured stresses had little correlation between subregions of the map [46]. In the same study, stress maps were filtered to show regions with mean stress within an arbitrary stress interval, indicating progression of damage with life fraction [46]. In another work, stress maps 1 $\times$ 1 mm with a step size of 8 μm were made of PS-PVD coatings after up to 300 thermal shock cycles, showing reduced stress and greater density of stress variation with thermal cycling [22]. Another study used a larger laser spot size to average many alumina crystal grains, producing stress maps with 400 μm resolution and covering a larger area of 40 $\times$ 8 mm for TBC samples after various thermal and mechanical loadings [15]. The stress maps described so far showed stress distribution within the plane of the TGO, acquired nondestructively with the TGO morphology inferred; PLPS has also been used on prepared cross-sections to explicitly show stress variation with TGO morphology. Cross-section PLPS stress maps with resolution of around 2 μm have been made, clearly showing more compressive stress at troughs in the TGO and less compressive at the crests [86].

The PLPS method is also able to capture local damage, since when the fluorescing volume encompasses both intact and cracked or delaminated TGO, distinct stress states result in more than one doublet that can be deconvoluted [15, 45, 78, 80, 83, 87]. Bimodal PLPS spectra have been deconvoluted to map local regions of damage, with the two stress states corresponding to intact and damaged TGO [15, 80]. The relative intensity of the stress-relieved luminescence signal relative to the total luminescence signal, referred to as bimodal fraction, has been used to indicate

accumulation of damage [45, 78], and the relative intensities of deconvoluted spectra have been used to represent area fractions of damaged and undamaged regions [83].

PLPS Collection Procedure

Photoluminescence measurements were taken with a Princeton Instruments Acton SP 2150 spectrometer with 1200 grooves/mm grating, a PIXIS 100B charge-coupled device (CCD), a Laserglow 532 nm diode laser, and an RPB Raman probe with fiber optic cables. Calibration was done with a neon-argon source lamp, achieving root mean square error less than 0.020 nm. A block of polycrystalline alumina was used to ensure laser perpendicularity with the sample holder by verifying that the intensity of the R lines did not change significantly between the four corners and the center of the block. The alumina block was then replaced in the sample holder with the sample. This procedure was repeated before each tested sample.

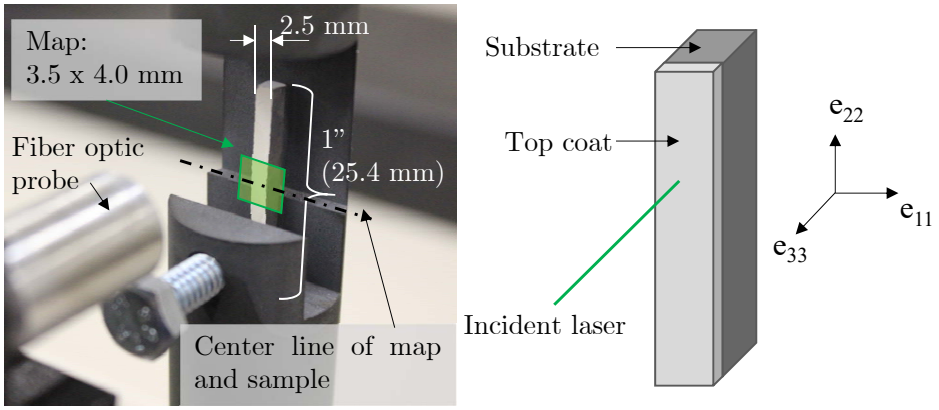

Figure 3.4: Experimental setup for stress maps by photoluminescence spectroscopy.

For data acquisition, the laser power was increased to 30 $\pm$ 1 mW, and focusing was achieved by adjusting the probe-to-sample distance until the intensity of the R lines was maximum without saturating the detector. Due to the varying TGO thickness between samples, the exposure time

was adjusted for each sample, in the range of 100 to 400 ms. Four accumulations per point were collected and averaged to reduce the influence of transient effects. For each sample, a map of 3.5 x 4.0 mm was made vertically centered on the sample slice, as shown in Figure 3.4, with a step size of 100 μm, for a total of 1400 pixels per map. The step size was smaller than the laser spot size, which was about 200 μm. The map width was wider than the sample width to ensure that data was collected across the entire width of the sample, including the edges, and data from beyond the sample edges was discarded in post-processing. Data collection was performed in LightField software [88] with acquisition and automated stage movement coordinated by a MATLAB [89] script.

PLPS Analysis Procedure

The PL spectra were restricted to the range of 14300 to 14500 cm^{-1}, then the baseline was fit with a linear function and removed. Any spectrum that had saturated or had a signal to noise ratio below 15 was not passed to the fitting code; these pixels are represented as white in the contour maps. Each spectrum was first fit in "single mode," using one doublet of R lines under the assumption of a single distinct stress state. The goodness of fit (GoF) was calculated using the normalized root mean square error, and any spectrum with a GoF below 0.99 was then fit bimodally. Bimodal fitting uses two R line doublets, assuming that the area producing the PL signal encompasses an area with two distinct stress states, one with greater stress and one stress-relieved. The goodness of fit was again calculated, and the fit with the higher GoF value kept. Figure 3.5a shows an example spectrum fit singly; a good fit is not achievable. The same spectrum is fit bimodally in Figure 3.5b, and a much better fit is achieved.

Bimodal fitting was used for all samples regardless of thermal history, as there are numerous reasons a given spectrum could have multiple stress states. A second, stress-relieved doublet can be

the result of local cracking or delamination, indicating damage to the TGO [22, 45, 90]. Variation in the morphology and phase composition of the alumina can also cause bimodality. While α-alumina has a continuous morphology and is constrained, with higher stress, θ- or γ-alumina has a whisker morphology and is unconstrained, with lower stress [9, 45]. In early-life TBCs, such as the uncycled samples, the alumina has not fully transformed from amorphous to transient phases (such as θ and γ) to the metastable α form, so this variation in phase is possible. In samples of all lifetimes, spatial variation in stress state may arise from the varying geometry of the TGO layer. Lengthening and rumpling of the TGO relieves its compressive stress, and the growth of the TGO has local variation [22]. Increased rumpling can be caused by local gaps in the YSZ columns, which constrains the TGO less [46]. The formation of spinels and other undesirable non-alumina oxides can cause local cracking, causing stress relief [22].

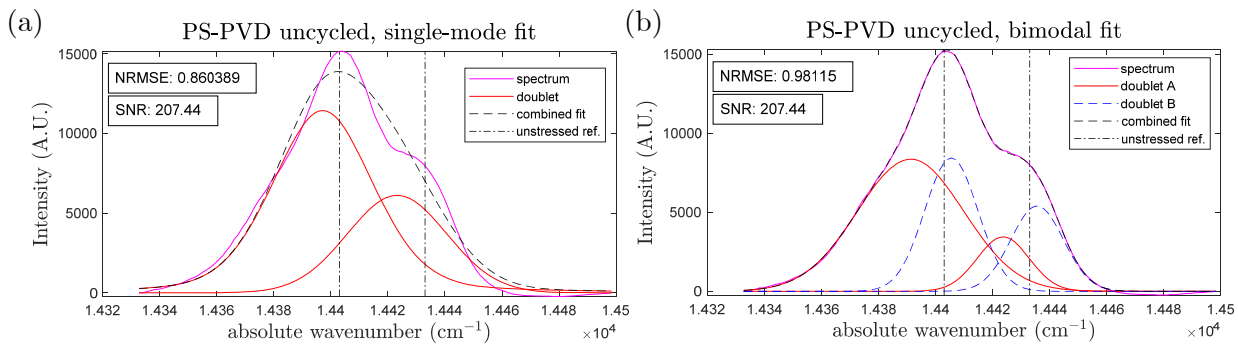

Figure 3.5: Example spectra fit with a single doublet (a) and with a pair of doublets (b).

Fitting is done by a least-squares fit of a pair of pseudo-Voigt functions to the data, with constraints applied to the following properties: R2/R1 area ratio, R2/R1 full width at half maximum (FWHM) ratio, and separation of the R1 and R2 peaks. The four parameters to be fit for each peak (area, position, FWHM, and Lorentzian fraction) were also restricted between upper and lower bounds. In the case of bimodal fitting, two pairs of pseudo-Voigt functions are summed. It is necessary to

constrain the fitting such that the R lines obey known trends and stress dependencies; otherwise, the fit may be incorrect, despite good statistical agreement with the data [78, 80].

The separation between the R1 and R2 peaks is linearly dependent on the biaxial stress as measured by the R2 peak position [78, 80]. This relationship was found by [80] to be of the form

$$\text{separation} = 29.923 - 0.155\Delta\nu_{\text{R2}} \tag{3.5}$$

where $\Delta\nu_{\text{R2}}$ is the position of R2 in cm^{-1}, with a standard deviation of 1.0 cm^{-1}; the samples used to derive this equation were EB-PVD YSZ on CMSX-4 substrates with Pt-Al or Pt diffusion bond coats, similar to the samples in this work. A similar relationship was derived by [78], also on EB-PVD coatings, of the form

$$\text{separation} = 30 + 0.82\sigma \tag{3.6}$$

where σ is biaxial compressive stress calculated from the R2 position. These two equations produce peak separations which differ by less than 1% in the range of 6 GPa compressive to 6 GPa tensile. Equation 3.5 was used in this work, with the peak separation constrained to ± 1 cm^{-1} based on the R2 position. When determining stress from spectral data, the R2 peak is preferred, as it is insensitive to deviatoric stress and so indicates mean stress [70]. The following relationship is used:

$$\sigma_{biaxial} = \frac{\nu_{R2} - \nu_{\text{R2, ref}}}{\text{PSC}} \tag{3.7}$$

where ν_{R2} is the fitted position of R2 in cm^{-1}, $\nu_{R2,\,ref}$ is 14432 cm^{-1}, and PSC is the coefficient 5.073 cm^{-1}/GPa^{-1}.

When producing maps of the stresses and calculating average and standard deviation, only spectra with sufficiently high GoF were considered. The minimum acceptable GoF varied depending on the average SNR of the sample. The minimum GoF for inclusion was typically 0.99 and was always above 0.95, with the exception of the uncycled EB-PVD samples that had very low SNR. In addition, pixels outside a given column range were excluded, due to the mapped region being wider than the sample. R lines were still able to be collected when the laser was just next to but not on the sample, due to the large spot size and reflection of the light from the exposed substrate on the cut edge, but these had much lower fitting quality and clearly erroneous stress results. Figure 3.6 shows a pair of maps of the same sample with and without discarding the extra pixels. Pixels near the edges were also excluded to eliminate edge effects when reporting stress results.

Table 3.2: Example of effect of limiting map data on reported statistics.

	Avg. GoF	Avg. A Stress (GPa)	Avg. B Stress (GPa)
Full Map	0.9885	−2.20	−1.28
Restricted Map	0.9927	−2.37	−1.45

The goodness of fit map shows that the pixels off the sample have a much lower fit quality, and the stress in these pixels is much less compressive and sometimes tensile. Table 3.2 illustrates how the extraneous pixels skew the map statistics. White pixels represent pixels that have been discarded for one of the following reasons: not fit due to saturation or SNR below 15; resulting fit with GoF too low; or outside specified column range and therefore affected by edge effects.

For each fitted spectrum, the overall stress was calculated by averaging the A and B stresses

weighted by their area fraction, as expressed in Equation 3.8.

$$\sigma_{avg} = (\frac{area_B}{area_{total}})(\sigma_B) + (1 - \frac{area_B}{area_{total}})(\sigma_A) \tag{3.8}$$

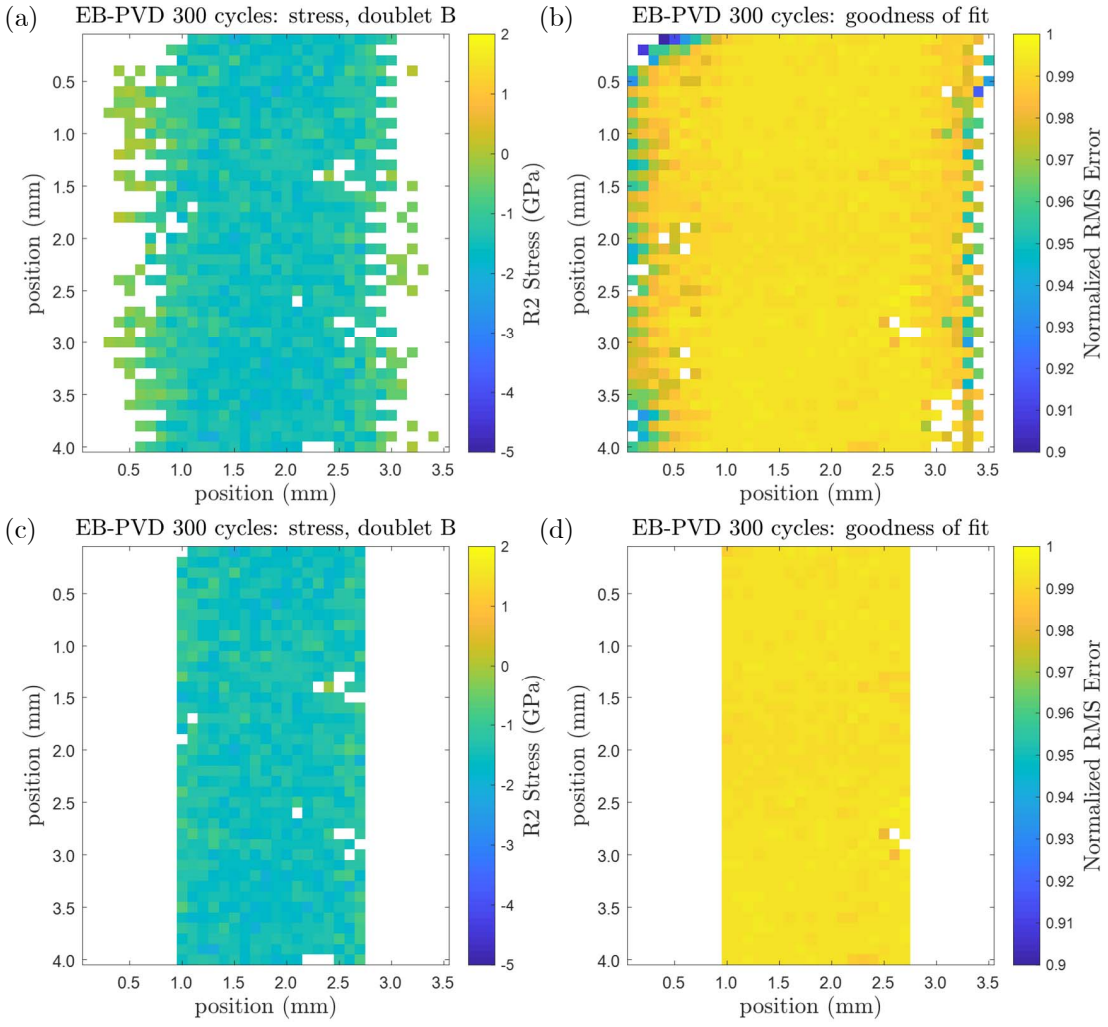

Figure 3.6: Complete maps showing doublet B stress (a) and goodness of fit (b), compared to the same maps with edge data discarded (c and d, respectively). Note that the goodness of fit scale is displayed from 0.9 to 1.

Scanning Electron Microscopy

Scanning electron microscopy (SEM) is a powerful tool for producing images at much higher magnification than can be achieved with conventional light microscopy, typically having a resolution between 1 and 10 nm [91]. SEM imaging of a polished cross section of a TBC reveals details of the coating's microstructure, such as column size, shape, and porosity, thickening and rumpling of the TGO, phases of the bond coat, and cracking and delamination.

SEM cross-section images have been used with image analysis to quantify column widths, intercolumnar gap widths, and porosity of PS-PVD samples [14]. SEM has been used to characterize the microstructure of PS-PVD coatings, such as column shape, degree of branching, porosity, and changes in microstructure in the growth direction, to study the mechanism of deposition; in combination with transmission electron microscopy and selected area electron diffraction, these studies have lead to the explanation of deposition by nanoclusters as well as adatoms [20, 23]. SEM has been used to study the thickening of the TGO, increased convolution of the TGO, and cracking and delaminations in the coating with thermal cycling [46, 93, 94]. Observations of TGO thickness with thermal exposure has demonstrated that TGO growth is diffusion-controlled and follows parabolic growth, and growth constants have been calculated [93], and SEM images have been used to study the growth of the intermixed zone and fully dense zone of the TGO [95]. The tendency of cracks and delaminations to be generated near the crests of the TGO has contributed to the understanding of TGO roughness as a key feature leading to spallation failure [4, 48], and observation of cracks in TGO crests have provided an explanation for decreased TGO stress with thermal cycling [93]. Additional processes contributing to failure that have been observed via SEM include cracking of the TGO, preferential oxidation along the bond coat grain boundaries, widening of cracks into cavities, depletion of Al near the TGO, and formation of oxides other than alumina within the bond coat or TGO [48, 82, 93].

CHAPTER 4: PIEZOSPECTROSCOPIC INVESTIGATION

Photoluminescence Piezospectroscopy of Thermally Grown Oxide

Objectives

Stress relief in the TGO may be caused by the TGO lengthening as the bond coat rumples, but is also a sign of cracking and damage. TGO stress evolution is therefore an indicator of damage accumulation. TGO residual stress was evaluated for samples at three lifetimes for both PS-PVD and EB-PVD to provide insight into the extent of damage accumulation. The residual stress measured is primarily type I, stress developed in multiple grains. The sources of this stress are macroscopic — the thermal expansion and contraction during thermal cycling which is constrained by the substrate, growth of new alumina at the interfaces and between existing alumina grains, and initiation and propagation of cracks and delaminations.

Stress evolution of PS-PVD samples

A representative set of stress maps for the PS-PVD samples is shown in Figure 4.1 [36]. The top row maps are of the more-stressed doublet, doublet A, which corresponds to intact TGO. The middle row maps are of doublet B, which corresponds to cracked or delaminated TGO. The bottom row maps are of the weighted average stress, which is representative of the fluorescing volume as a whole and is more readily comparable to results from characterization methods that cannot distinguish between the two regions.

The TGO of the PS-PVD samples were most compressive when uncycled, with stress in the expected range of EB-PVD coatings in the first several hours of thermal cycling [47, 78, 98, 99].

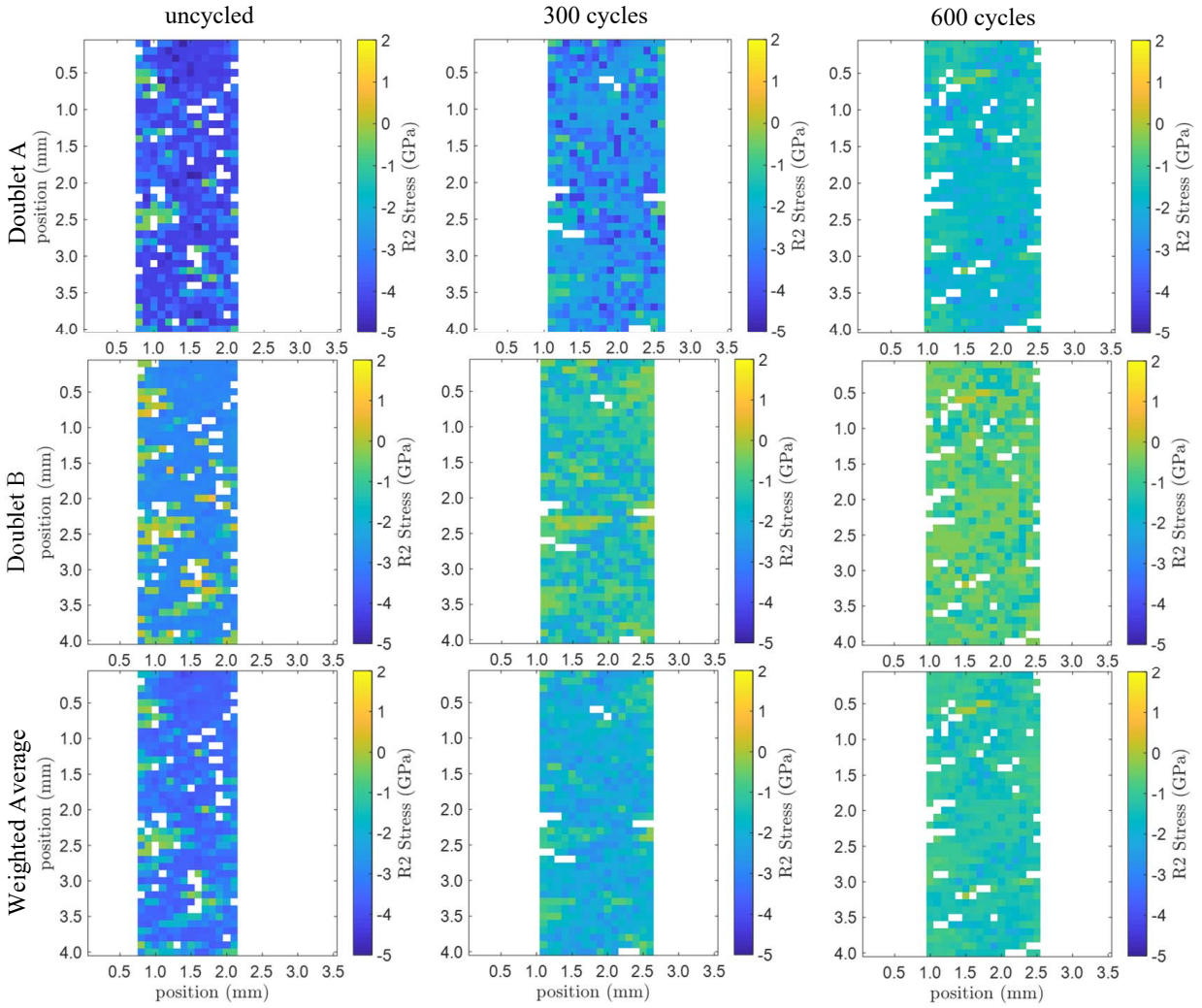

Figure 4.1: Representative TGO residual stress maps for both doublets and the weighted average of the doublets for PS-PVD samples after 0, 300, and 600 thermal cycles.

The 1 hour heat treatment that was done to restore oxygen content also allowed a continuous TGO to develop of sufficient thickness for PL analysis. There are small regions of tensile stress up to 0.9 GPa in the doublet B map for uncycled; these may correspond with crests or asperities in the TGO [4]. Stress became less compressive with increased cycling, as expected from literature [22, 36, 46, 47]. The average residual stresses and average spatial variation in GPa are reported in Table 4.1 [36].

Table 4.1: Average residual TGO stress for PS-PVD samples (GPa); $\pm$ values represent the average spatial variation in a sample, where the spatial variation of a sample is the standard deviation of stress values in a map.

	Uncycled	300 Thermal Cycles	600 Thermal Cycles
Doublet A	-3.87 ± 0.99	-2.75 ± 0.98	-1.97 ± 0.36
Doublet B	-2.49 ± 1.14	-1.22 ± 0.62	-0.89 ± 0.37
Weighted Average	-3.04 ± 0.92	-1.69 ± 0.56	-1.33 ± 0.28

Between 0 and 300 cycles, the amount of stress relief was over 1 GPa for both doublets and the weighted average stress, and between 300 and 600 cycles the stress relief was less, about 0.4 GPa for the weighted average stress. The spatial variation per map (as measured by standard deviation of pixels in a given map) slightly decreased with thermal cycling. [36]

Stress evolution of EB-PVD samples

A representative set of stress maps for the EB-PVD samples is shown in Figure 4.2 [36]. Because the TGO in the uncycled EB-PVD samples was very thin and not continuous, the signal-to-noise ratio was much lower, and fewer pixels were successfully fit. Because so few spectra were able to be fit, the map cannot be assumed to be representative of the whole sample, though the spectra that were successfully fit produced stress values in the expected range [36].

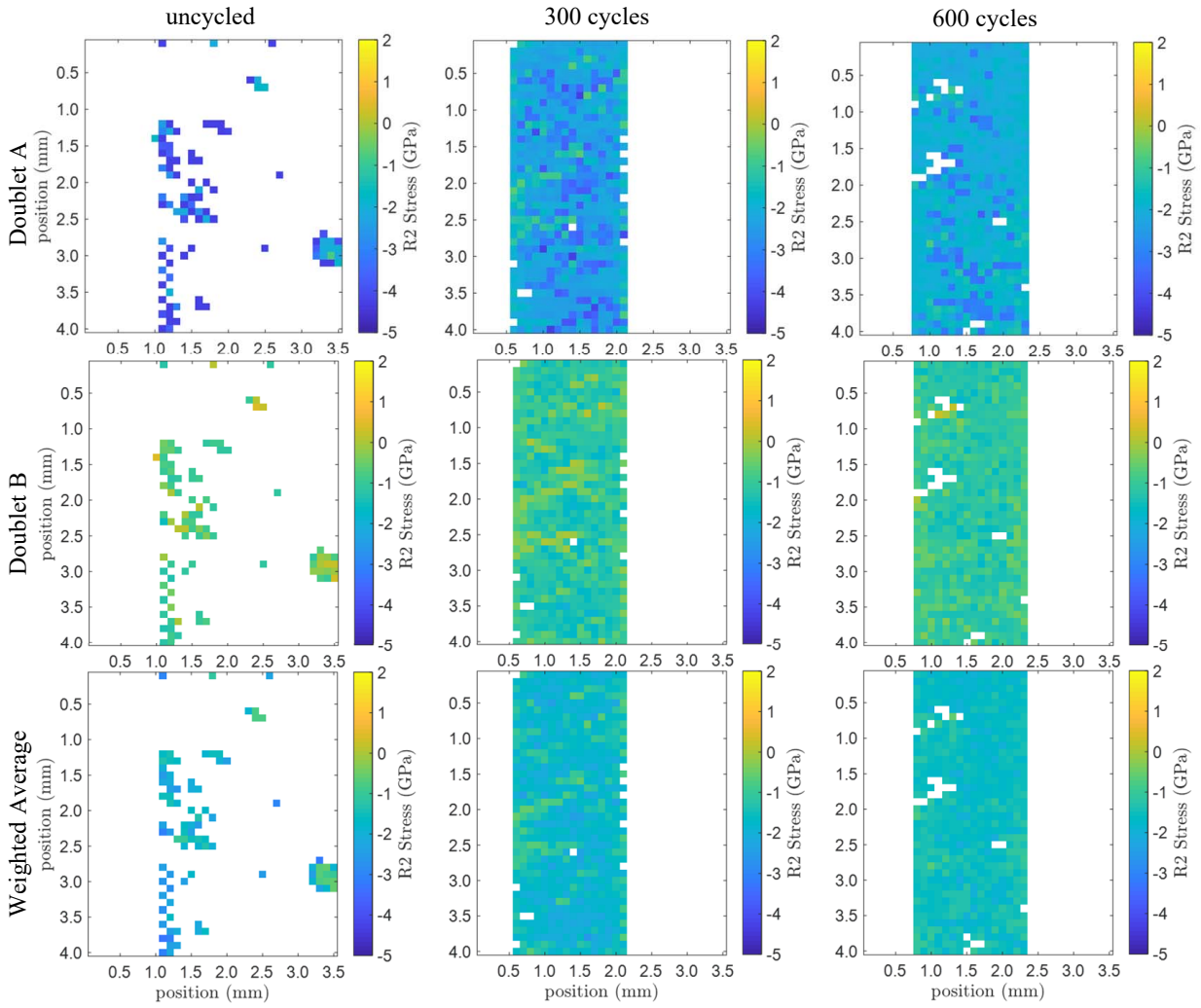

Figure 4.2: Representative TGO residual stress maps for both doublets and the weighted average of the doublets for EB-PVD samples after 0, 300, and 600 thermal cycles.

The EB-PVD samples' TGO were in compression, and became less compressive with thermal cycling. There are some regions of mild tensile stress (about 0.13 GPa) in the doublet B map at 300 cycles, which again may correspond to crests and asperities in the TGO [36]. The average residual stresses and average spatial variation in GPa are reported in Table 4.2 [36].

Table 4.2: Average residual TGO stress for EB-PVD samples (GPa); $\pm$ values represent the average spatial variation in a sample, where the spatial variation of a sample is the standard deviation of stress values in a map.

	Uncycled	300 Thermal Cycles	600 Thermal Cycles
Doublet A	-3.94 ± 0.92	-2.40 ± 0.46	-2.15 ± 0.40
Doublet B	-0.91 ± 0.47	-1.41 ± 0.33	-1.20 ± 0.29
Weighted Average	-2.28 ± 0.57	-1.68 ± 0.28	-1.52 ± 0.21

Between 0 and 300 cycles, the doublet B stress increased by about 0.5 GPa. This increase may be due to growth stresses arising from the constrained rapid growth of the TGO in the early thermal cycles; TGO stress is expected to increase in the first several hours of thermal exposure. In contrast, the doublet A stress decreased by 1.5 GPa, as is expected for TGO stress after the first several hours [46, 47], and the weighted average stress decreased by about 0.5 GPa. The change between 0 and 300 cycles includes both the initial sharp increase of stress and the stress relief that occurs after the first several cycles. However, the overall trend between 0 and 300 cycles is not reliable due to the very few fittable spectra for the uncycled sample (fewer than 10% of spectra within the column range could be fit, whereas for the other samples, typically around 90% of spectra could be fit). Between 300 and 600 cycles, the average $\Delta\sigma$ for both doublets and the weighted average was about 0.25 GPa. The spatial variation of stress slightly decreased between 300 and 600 cycles [36].

Comparison of PS-PVD and EB-PVD

A summary of the average stresses is shown in Figure 4.3. Doublet A corresponds to the stress in the intact TGO, which is relieved due to lengthening of the TGO during thermal cycling. Doublet B corresponds to the stress in microcracked or delaminated TGO, which is relieved due to lengthening as well as further crack initiation and propagation. The weighted average stress includes the

stress from both doublets, weighted by their fractional area. This stress represents the overall stress state of the fluorescing volume.

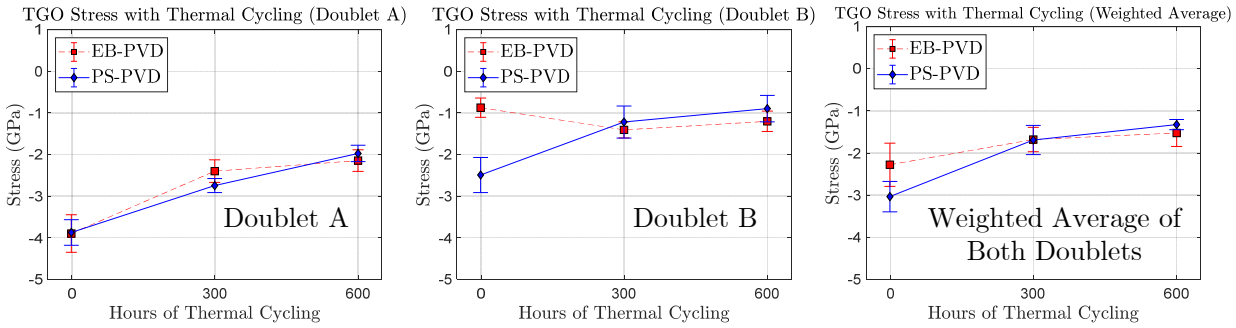

Figure 4.3: Summary of residual TGO stress values for the higher-stressed doublet (designated doublet A), the lower-stressed doublet (doublet B), and the average stress of both doublets weighted by their area fraction. Each data point is the average of the samples of a given combination of coating method and cycling history. Scatter bars indicate one standard deviation among the average stress of the samples.

The uncycled samples had the greatest residual stress, as expected. Both coating types had very similar stress for doublet A, around 4 GPa compressive, but showed very different stress in doublet B. The uncycled PS-PVD samples, which had a 1 hour heat treatment to achieve stoichiometry, had much higher doublet B stress (around 2.5 GPa compressive) than did EB-PVD, which had no heat treatment. The EB-PVD samples' lower stress regions may be areas of little TGO growth, as the growth has spatial variation and the samples have had no thermal exposure other than the high temperature during the EB-PVD process [36]. The weighted average stress for both coating types was in the expected range for the TGO of EB-PVD and PS-PVD samples in the first several hours of thermal cycling [22, 47].

Between uncycled and 300 cycles, the PS-PVD samples showed significant stress relief of more than 1 GPa for both doublets and the weighted average. Stress relief may occur as the TGO is allowed to lengthen from roughening of the bond coat, or may be a result of local microcracking, indicating damage [22].

After 300 cycles, the EB-PVD and PS-PVD samples had similar stresses, with PS-PVD having sightly higher compressive stress ($\Delta\sigma = 0.35$ GPa) for one doublet and slightly lower ($\Delta\sigma = 0.19$ GPa) for the other, and the weighted average stress being nearly exactly the same (1.7 GPa compressive). Between 300 and 600 cycles, the PS-PVD samples experienced further stress relief, though the difference was less than that between uncycled and 300 cycles. The average PS-PVD stress relief between 300 and 600 cycles was about $\Delta\sigma = 0.5$ GPa, compared to more than 1 GPa of relief between uncycled and 300 cycles. The EB-PVD samples experienced a smaller amount of stress relief from 300 to 600 cycles; the average stress relief was about $\Delta\sigma = 0.2$ GPa. The PS-PVD samples also had lower residual stress by about 0.2 GPa than did the EB-PVD samples after 600 cycles. Despite the PS-PVD samples having slightly lower stress, the stress in the two coating types was quite similar.

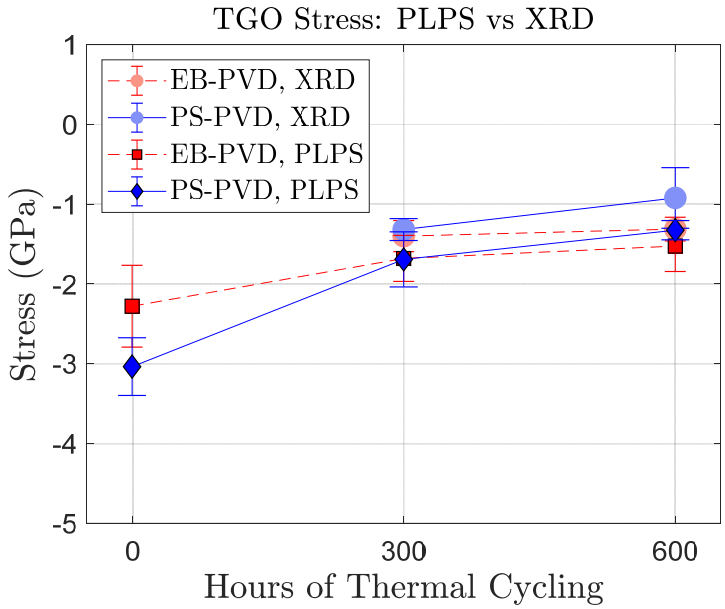

Figure 4.4: Average TGO stress as measured by PLPS (using weighted average) and by synchrotron XRD at room temperature. Scatter bars represent the standard deviation among samples of a given coating type and thermal history.

Stress measurements of the TGO were also performed using synchrotron X-ray diffraction during a thermal cycle at the Advanced Photon Source at Argonne National Laboratory, with results re-

ported elsewhere [56]. Room temperature strain results from that study were converted to stress (details in Appendix) for comparison to the TGO stress results from PLPS, shown in Figure 4.4. The results for the cycled samples are in good agreement. The TGO layers of the uncycled samples were too thin to obtain sufficiently high diffraction intensity for fitting and are not reported [56].

After both 300 and 600 cycles, the PS-PVD samples had greater variation between samples than the EB-PVD samples. This is likely because the EB-PVD samples were coated in a single deposition run, whereas the PS-PVD samples were coated in multiple runs, and PS-PVD today has greater process variability. Both PS-PVD and EB-PVD samples had increased uniformity (variation of stress across a given sample) with greater cycling time [36].

The stress relief in both coating types can be attributed to lengthening of the TGO as the TGO/bond coat interface becomes more rumpled and to microcracking in the TGO relieving the compressive stress [36]. SEM results in Chapter 5 show support for both of these causes of stress relief.

Raman Spectroscopy of Yttria-Stabilized Zirconia

Objectives

Residual stress in the YSZ top coat drives crack initiation and propagation in the top coat, which may lead to spallation failure; increased residual top coat stress is also an indicator of loss of strain tolerance due to sintering. The presence of the monoclinic zirconia phase affects the mechanical properties and stress state of the top coat, and is undesirable due to its lower fracture toughness and its ability to transform to the tetragonal phase during thermal cycling, causing additional stress in the coating. YSZ stress was measured and the presence or absence of the monoclinic phase was observed for samples at three lifetimes for both PS-PVD and EB-PVD to gain insight into their propensity for cracking and sintering. The residual stresses measured are types I and II

(stresses developed in multiple grains and within one grain, respectively). Some of the sources of residual stress are thermal expansion and contraction during thermal cycling constrained by the substrate and by connections between columns and grains due to sintering, transformation between monoclinic and tetragonal phase with associated volume change, and initiation and propagation of cracks.

Phase analysis via Raman spectroscopy

Representative spectra from PS-PVD and EB-PVD cycled samples as well as the powders used to make them are shown in Figure 4.5. All samples of both coating types exhibited the six characteristic peaks of the tetragonal/ tetragonal prime zirconia phase at around 148, 260, 320, 460, 610, and 640 cm^{-1}, marked "t". All PS-PVD samples also strongly exhibited the two characteristic peaks of the monoclinic zirconia phase (at around 182 and 191 cm^{-1}, marked "m"). The powder used to make the PS-PVD coatings, consisting of a mechanical mixture of ZrO_2 and Y_2O_3, exhibited both the characteristic monoclinic and tetragonal phases; the tetragonal peaks were much weaker than for the coatings [36]. The 8SYZ powder used to make the EB-PVD feedstock ingots had very clear tetragonal peaks, and also had the characteristic monoclinic peaks, though these were very weak. Both powders had smaller peaks at 374, 383, 504, 525, 557, and 577 cm^{-1}, most of which are identified as monoclinic zirconia and some of which may be a cubic spinel [100, 101]. The cubic zirconia phase is not identified, as Raman spectroscopy has very low sensitivity to the cubic zirconia phase [62].

The presence of monoclinic phase in the PS-PVD samples, especially in the uncycled samples, may be due to powder particles incompletely melted or vaporized during deposition [102], due to insufficient mixing of vaporized ZrO_2 and Y_2O_3 [7], or to a combination of the two causes. Transformation from tetragonal prime to monoclinic upon cooling is undesirable, as the transformation

is accompanied by a 4–5% volume increase, imparting strain to the coating [43]. Monoclinic phase in the initial as-deposited state is undesirable, as it can transform to tetragonal upon heating, again with a volume change that strains the coating [103], and it has lower toughness than tetragonal phase [104], providing lower resistance to cracking. Monoclinic phase being present in the PS-PVD samples but not the EB-PVD suggests that the PS-PVD samples may be more susceptible to cracking in the YSZ, especially near the crack-prone region close to the TGO and bond coat [36].

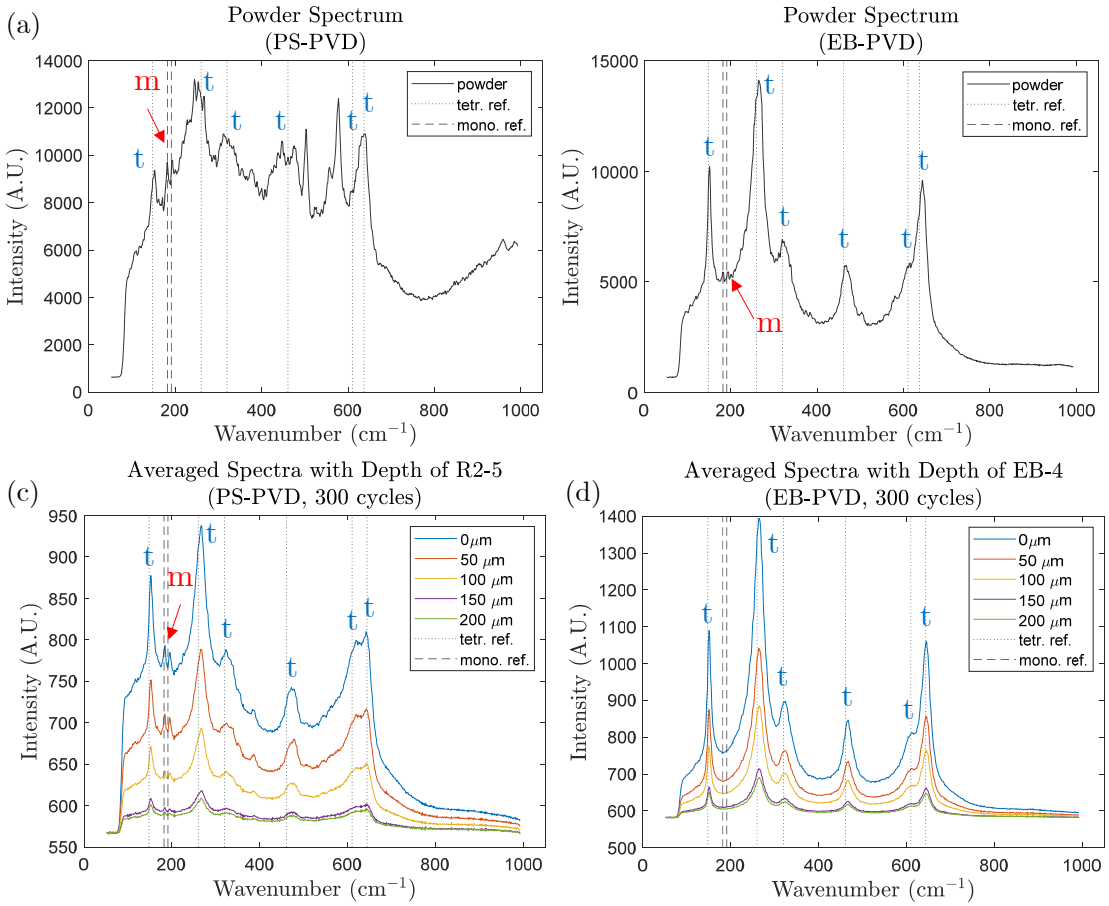

Figure 4.5: Raman spectra of the powders used as stress-free references for PS-PVD (a) and EB-PVD (b) samples, and representative Raman spectra for PS-PVD (c) and EB-PVD (d) coatings after 300 thermal cycles.

YSZ stress evolution via Raman spectroscopy

Results of the YSZ residual stress with depth and its evolution with thermal cycling are shown in Figure 4.6 [36] and residual stresses at the surface are listed in Table 4.3 [36].

Table 4.3: Average and standard deviation of residual YSZ surface stress among samples of a given coating type and thermal cycling.

	Average (MPa)	Standard Deviation (MPa)	# of Samples
EB-PVD, uncycled	472	122	2
PS-PVD, uncycled	−8.7	100	6
EB-PVD, 300 cycles	−173	20	2
PS-PVD, 300 cycles	−261	28	4
EB-PVD, 300 cycles (outlier)	262	–	1
EB-PVD, 600 cycles	−305	15	3
PS-PVD, 600 cycles	−352	31.2	4

In all samples, the variation of stress with depth (the difference between the stress at 0 and 200 μm below the surface) was small, on average 55 $\pm$ 28 MPa and at most 145 MPa. This variation is smaller than that reported in much of the literature, in which the variation is often between 300 and 600 MPa for both coating types [6, 64, 105–107], but some authors have reported variations less than 200 MPa [55, 66]. In general, stress became more compressive closer to the TGO interface, attributed to the pressure from the constrained volumetric expansion of the TGO [108, 109] as well as lower porosity and hence higher elastic modulus closer to the interface [36, 105, 110–112].

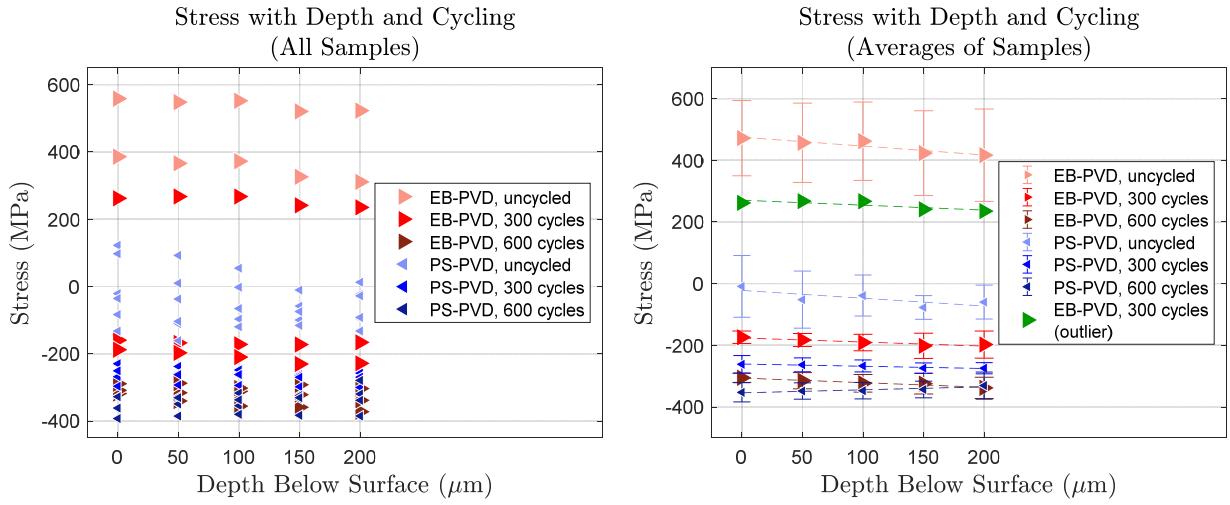

Figure 4.6: Average YSZ stress with depth and cycling time for PS-PVD and EB-PVD. Plot (a) shows data points for each sample. In plot (b) data points represent the mean value among samples of the same coating type and thermal history, with scatter bars representing the standard deviation among those samples. An outlier sample for EB-PVD at 300 cycles is plotted separately. Dashed lines are a linear fit of the data points.

The residual stresses of the uncycled samples were very different between the two coating types — slightly compressive for PS-PVD and moderately tensile for EB-PVD. The PS-PVD uncycled coatings were more compressive than expected from comparison to the literature, but this is attributed to the one hour heat treatment given to restore oxygen content, whereas the referenced study did not require a heat treatment because they supplied additional oxygen during deposition [22]. The volume expansion of the TGO during this heat treatment applied compressive stress on the top coat [108, 109]. The uncycled EB-PVD samples had tensile stress of around 470 MPa. This was more tensile than expected, as the as-deposited stress is often compressive in the literature [66, 106] and compressive stress is expected during cooling from high temperature due to the metallic substrate having greater thermal contraction than the ceramic, but tensile as-deposited

stress has been reported before, up to about 200 MPa [64]. For the same thermal mismatch strain during cooling after deposition, the residual stress is partly determined by the in-plane modulus, which is affected by the microstructure, especially the packing density of the columns [113]. A potential reason for the unexpected tensile stress is the highly localized nature of the Raman stress measurements; though twenty locations were averaged together across a 2.5×4.0 mm^2 area, each individual measurement location was smaller than a single column.

The YSZ top coats of both EB-PVD and PS-PVD coatings became more compressive with increased thermal cycling, consistent with the literature [22, 114, 115]; this is attributed to the volume increase of the growing TGO subjecting the top coat to compression [108, 109] as well as reduction of the Young's modulus due to sintering forming contacts between the columns and thereby increasing the apparent Young's modulus [43, 116]. After 300 cycles the PS-PVD samples were in close agreement at around 250 MPa compressive, and two of the three EB-PVD 300 cycle samples were around 170 MPa compressive with close agreement with each other. The third sample of the EB-PVD 300 cycle set was quite different, about 260 MPa tensile. The reason for this discrepancy is not yet known.

After 600 cycles both coating types had similar compressive stress at the surface, around 300 MPa for EB-PVD and 350 MPa for PS-PVD, which is within the expected range for thermally cycled EB-PVD samples [105] and PS-PVD samples [22]. While the EB-PVD coatings were more stressed with depth as expected, the PS-PVD coating stress was relieved with depth. This indicates that at high lifetimes PS-PVD had more stress relief from cracking near the TGO interface [36]. For both coating types, the stress change between 0 and 300 cycles was greater than that between 300 and 600 cycles. This is likely because the thickening of the TGO and occurrence of sintering is most rapid at the beginning of thermal cycling, as the rate of TGO growth [30] and the rate of sintering [112] each scale with the square root of hot time.

Conclusions

The PS-PVD coatings exhibited stress evolution similar to industry-standard EB-PVD coatings, while also having some different characteristics. These are summarized below.

- All PS-PVD samples contained monoclinic zirconia in their top coats, attributed to incompletely melted powder particles observed in SEM micrographs. The transformation between tetragonal and monoclinic phases during thermal cycling imparts additional strain into the coating and monoclinic zirconia has lower fracture toughness than the tetragonal phase, potentially causing more cracking in the YSZ. Monoclinic phase was not observed in any EB-PVD samples.

- PS-PVD top coats were slightly compressive in their uncycled state and became increasingly compressive after 300 and then 600 thermal cycles, consistent with the literature. EB-PVD top coats had similar stress for cycled samples, but were tensile in their uncycled state. The difference in the uncycled state between the coating types is likely due to the different temperatures during deposition and the different column microstructure, as well as the heat treatment applied to the PS-PVD coatings but not the EB-PVD coatings. The tensile as-deposited YSZ stress for the EB-PVD coatings is unusual but not unprecedented [64], and may be affected by the highly localized nature of the Raman measurements, which are smaller than a single column.

- PS-PVD top coat stress generally became more compressive with depth into the coating (closer to the TGO interface), though the stress gradient was lower than expected from literature. Unlike the other samples, the 600 cycle samples decreased in stress near the TGO interface; this is suspected to be due to the greater extent of cracking near the interface. The EB-PVD top coat stress became more compressive with depth for all samples, again

with a lower stress gradient than expected. The very small probed volume providing highly localized measurements likely affects the results and does not fully capture the effects of microstructural features such as intercolumnar gaps. Using a larger spot size is recommended for future Raman studies.

- TGO stress was bimodal, indicating two distinct stress states in the measured volume, for all samples of both coating types. The distinct stress states are attributed to TGO that is intact vs. cracked, or attached to bond coat vs. attached to top coat.

- TGO stress for the uncycled PS-PVD samples was compressive and in the expected range from literature (4 GPa for one doublet and 2.5 GPa for the other). The uncycled EB-PVD samples did not have sufficient TGO growth to obtain reliable measurements, though the few spectra that were fit indicated compressive stresses in the expected range (4 GPa for one doublet and 1 GPa for the other, and 3 GPa overall).

- The PS-PVD samples had TGO stress relief between 0 and 300 cycles, as expected. This is attributed to both TGO lengthening as the TGO/bond coat interface became convoluted as well as cracking and delamination at the TGO interface. SEM micrographs showed both increased convolution and greater extent of cracking, supporting this hypothesis. The cracking in the YSZ above the TGO is likely encouraged by the brittle monoclinic phase in the YSZ and by the highly convoluted shape of the TGO interface.

- The PS-PVD samples had further TGO stress relief between 300 and 600 cycles, though the stress difference was less than between 0 and 300 cycles. This stress relief is again attributed to TGO lengthening and further cracking. The EB-PVD samples also had stress relief between 300 and 600 cycles, though the stress difference was less than for PS-PVD.

- The PS-PVD TGO stress was similar to EB-PVD at 300 cycles and slightly less than EB-PVD at 600 cycles. SEM micrographs of both coating types at 600 cycles show extensive

cracking for both coating types, but the cracking is often within the TGO layer for PS-PVD and mostly at the TGO/YSZ interface for EB-PVD. The slightly lower TGO stress for PS-PVD may be due to the higher degree of cracking within the TGO layer rather than at the TGO/YSZ interface.

- The TGO stress for the cycled samples was in agreement with stress calculated from strain measurements made by synchrotron X-ray diffraction, providing additional support for the results.

Despite the numerous differences between the PS-PVD and EB-PVD samples, similar stress magnitudes and evolution with cycling were observed in both the YSZ top coat and the TGO. This is encouraging with regards to PS-PVD's suitability as a TBC deposition technique. Further observations and discussion of the microstructure and damage evolution will be presented in Chapter 5.

CHAPTER 5: SEM IMAGING

SEM Support for TGO Findings

The uncycled EB-PVD samples did not have enough TGO for stress mapping; only a few locations on the maps had spectra that were able to be fit. This is because the TGO was extremely thin, its only thermal exposure having been the high temperature during deposition. The average thickness of the TGO in the uncycled sample, shown in Fig. 5.1a, was 0.2 ± 0.1 μm as measured with image analysis, whereas for the 300 cycle sample in Fig. 5.1b the thickness was much greater, 3.4 ± 0.8 μm.

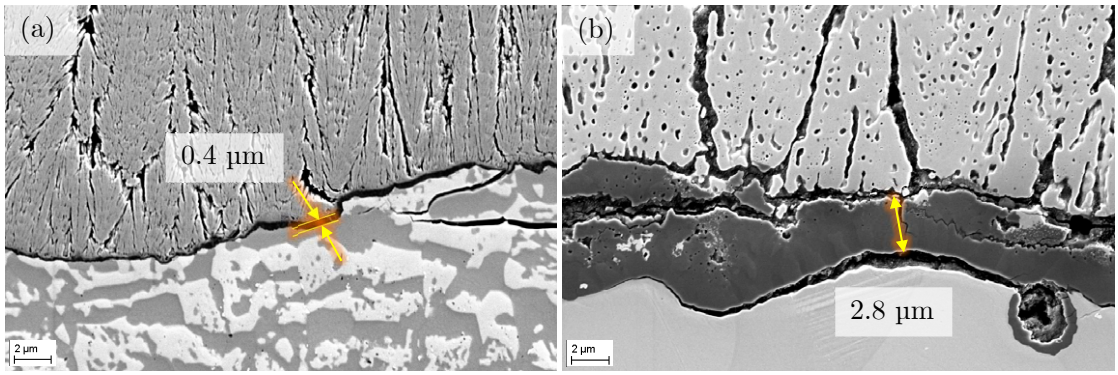

Figure 5.1: Cross-section SEM micrographs of an EB-PVD sample after 0 thermal cycles (a) and 300 thermal cycles (b), illustrating the increase in TGO thickness.

The uncycled PS-PVD samples, having received a 1 hour heat treatment, had a sufficiently thick TGO to produce complete stress maps. TGO thicknesses were measured using ImageJ software on SEM images and are reported for both coating types at all lifetimes in Figure 5.2.

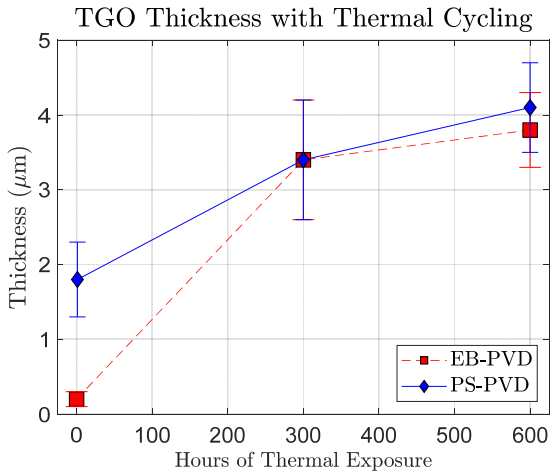

Figure 5.2: TGO growth with thermal cycling for both coating types. Error bars represent the standard deviation of thickness measurements in the SEM image used.

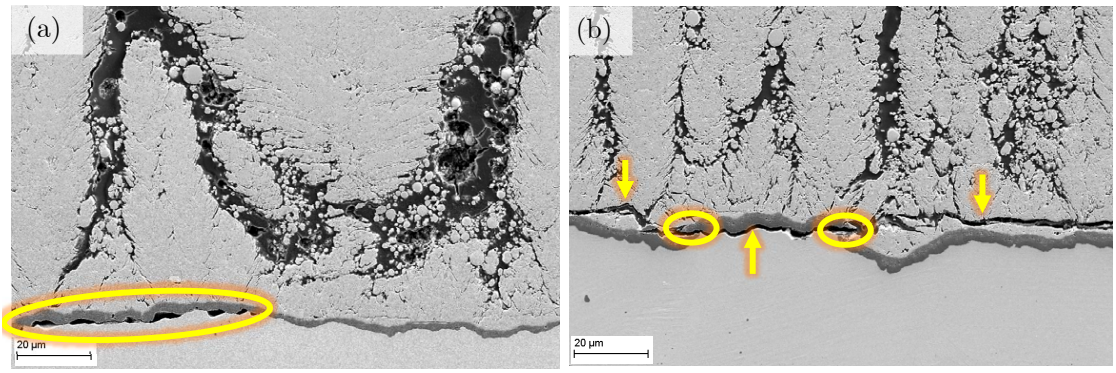

Figure 5.3: Cross-section SEM micrographs of an uncycled (a) and 300-cycled (b) PS-PVD sample. Cracks and delaminations are highlighted.

TGO stress in the PS-PVD samples was found to be relieved between 0 and 300 cycles. Figure 5.3 [36] compares cross sections from PS-PVD samples after 0 and 300 thermal cycles. Small delaminations between the TGO and bond coat, such as those circled in Figure 5.3a, may explain the significant spatial variation in the TGO stress maps. These delaminations occur under crests in the TGO, which is expected because these crests are the sites of out-of-plane tensile stress [4]. After 300 cycles, the TGO was both thicker and more convoluted; this convolution allowed the TGO to

lengthen, relieving compressive stress [36]. Increased convolution of the TGO is associated with cyclic creep in the bond coat during thermal cycling [4]. Cracking was also apparent after 300 cycles, marked with circles and arrows in Fig. 5.3b. The cracks likely originated at crests in the TGO due to the out-of-plane tensile stress there, which increases as the magnitudes of crests and troughs increases with thermal cycling [4]. The images provide support for the hypothesis that both TGO lengthening and local cracking contributed to the stress relief observed by spectroscopy [36].

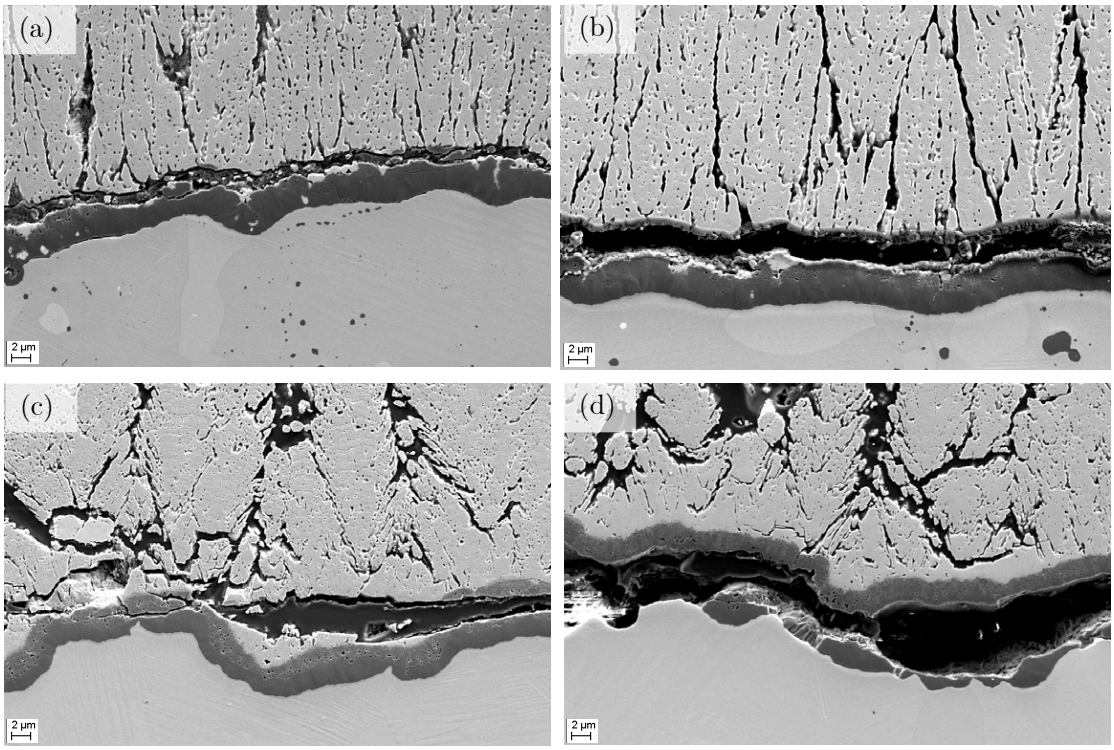

Figure 5.4: Cross-section SEM micrographs of an EB-PVD sample after 300 cycles (a) and 600 cycles (b), and a PS-PVD sample after 300 cycles (c) and 600 cycles (d).

Figure 5.4 [36] compares cross sections of both coating types after 300 and 600 thermal cycles. Cracking and delamination increased for both coating types, causing the stress relief reported in Chapter 4. However, the crack modes were different. Cracks and delaminations followed the

TGO/YSZ interface for the EB-PVD sample (Fig. 5.4a and b), likely because the interface was flatter and therefore did not divert the cracking to other paths. The delaminations being nearly exclusively at the interface may indicate lower adhesion strength for EB-PVD than for PS-PVD. The greater degree of convolution for the PS-PVD samples may be due to a rougher interface in the as-deposited state, or to the greater amount of defects and voids in the YSZ. The PS-PVD sample had cracking and delamination in the YSZ above the TGO as well as through and within the TGO, shown in Fig. 5.4c and d. The lower TGO stress in the PS-PVD samples compared to the EB-PVD samples may be due to the greater extent of cracking within the TGO itself [36].

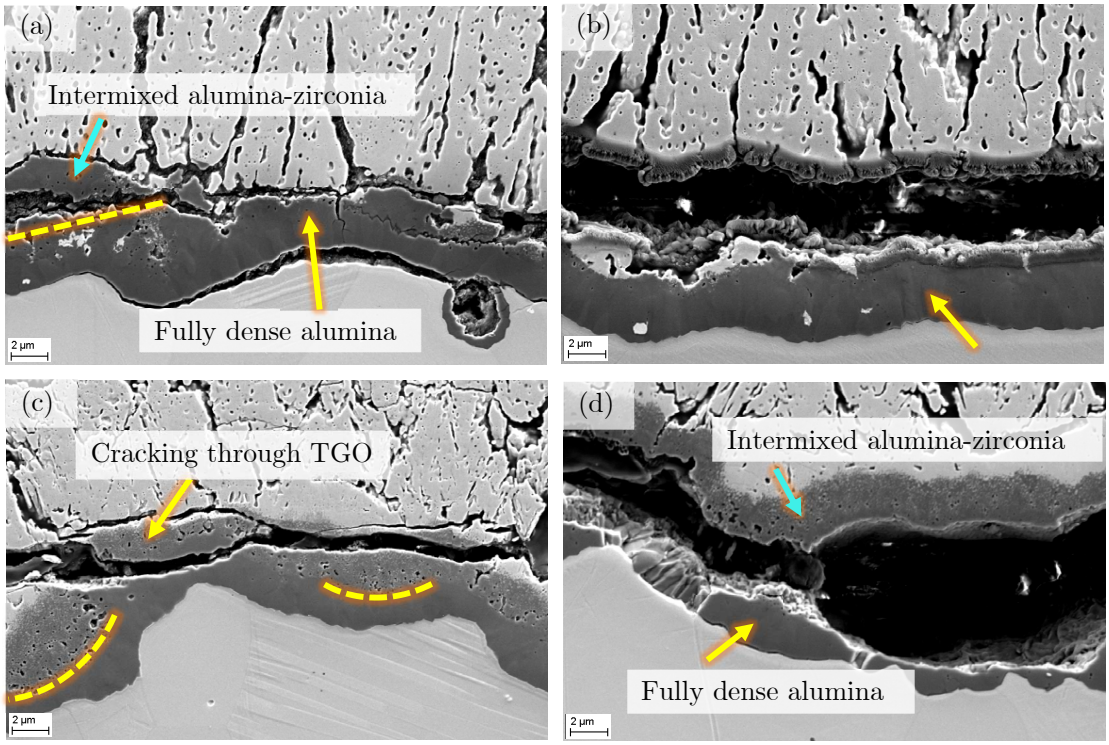

Figure 5.5: Cross-section SEM micrographs of an EB-PVD sample after 300 cycles (a) and 600 cycles (b), and a PS-PVD sample after 300 cycles (c) and 600 cycles (d). The intermixed zone and fully dense zone are marked with arrows, as is a location of cracking through the TGO. The dashed curves mark the interface between the intermixed zone and fully dense zone of the TGO.

Figure 5.5 shows the TGO more clearly, with the equiaxed zone of intermixed alumina and zirconia

and the columnar zone of fully dense alumina marked in Fig. 5.5a and d. The interface between these zones is marked in some places by dashed lines in Fig. 5.5a and c. The intermixed zone is more porous and therefore less resistant to cracking. The PS-PVD samples (Fig. 5.5c and d) had a greater fraction of intermixed zone compared to fully dense zone compared to the EB-PVD samples, which may be why the PS-PVD samples had more cracking within the TGO (Fig. 5.5c and d) rather than along the TGO/YSZ interface like in the EB-PVD coatings (Fig. 5.5a and b).

SEM Support for YSZ Findings

The monoclinic phase that was reported in Chapter 4 is attributed to unmelted particles and/or insufficiently mixed vapor during the PS-PVD process [7, 21, 102]. Unmelted particles were identified in SEM images (examples marked in Figure 5.6) which supports this conclusion. The particles frequently appeared in loose agglomerations with a gravel-like morphology (examples circled in Fig. 5.6a). The monoclinic phase has lower fracture toughness than the tetragonal phase [104]; along with the voids around the particles and defects such as those marked with arrows in Fig. 5.6a, this lowers the resistance of the PS-PVD topcoat to cracking. However, the greater porosity likely has the benefit of decreasing the thermal conductivity of the coating as well [4].

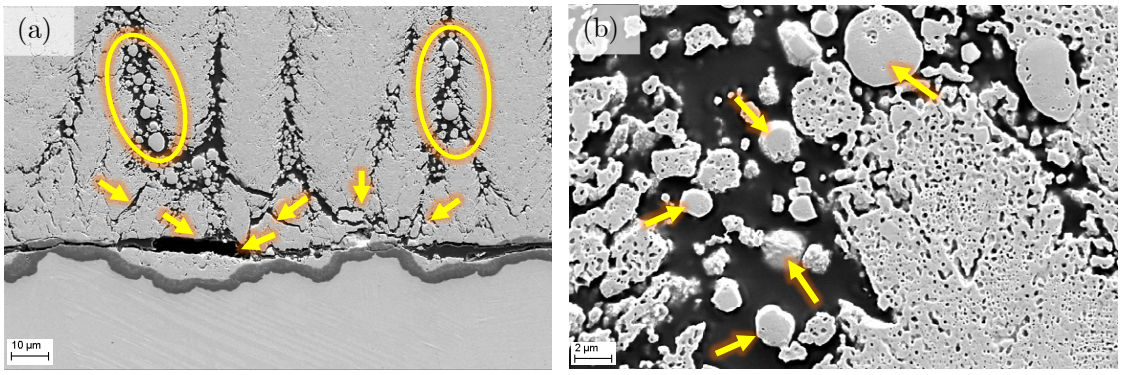

Figure 5.6: Cross-section SEM micrographs of a PS-PVD sample after 300 cycles at two magnifications. The circles in (a) indicated unmelted particles and the arrows indicate cracks and gaps. The arrows in (b) indicate unmelted particles.

Further Investigation of Coating Evolution and Damage Modes

The porosity and average pore size were quantified using ImageJ software with SEM images and the results are plotted in Figure 5.7. Porosity is in terms of area percent, and pore size is expressed as the area of the pore cross section in the image plane.

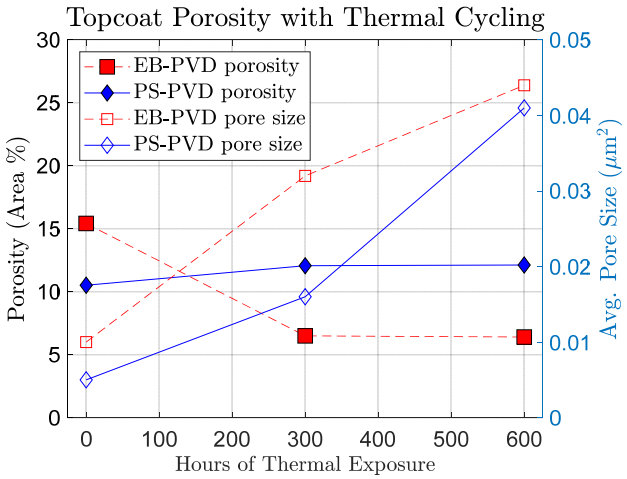

Figure 5.7: Change of porosity (left axis, solid markers) and average pore size (right axis, hollow markers) with thermal cycling.

For both coating types, the average pore size increased with thermal cycling due to pore accumulation, driven by reduction of surface area [116]. Porosity decreased with thermal cycling for the EB-PVD samples, which is expected as a result of sintering, but remained relatively constant for the PS-PVD samples. However, porosity for the PS-PVD samples is likely underestimated due to the difficulty of quantifying porosity in the regions of loose agglomerations of particles. These areas consist of particles surrounded by void rather than pores surrounded by YSZ; an example is shown in Figure 5.8.

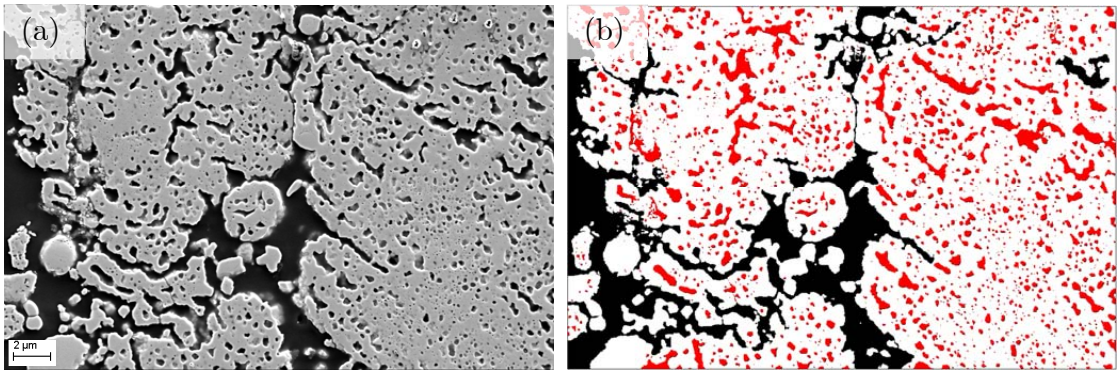

Figure 5.8: Cross-section SEM micrographs of a PS-PVD sample after 600 cycles (a) and the same image after thresholding and pore analysis (b). Pores included in analysis are colored red.

Images showing the evolution of intracolumnar pores for both coating types are shown in Figure 5.9. The size of the intracolumnar pores increased dramatically between the uncycled samples (Fig. 5.9a and b) and the samples with 300 cycles (Fig. 5.9c and d). Pores are expected to accumulate to form fewer, larger pores to reduce total surface energy. The pores in the EB-PVD samples (Fig. 5.9a, c, and e) appear in regularly spaced layers, a result of the rotation of the sample during deposition [116]. The pores in the PS-PVD samples (Fig. 5.9b, d, and f) are much less regularly spaced, likely because these substrates were stationary during deposition. The pores in the PS-PVD samples have a broader distribution of both size and shape than for EB-PVD, likely a consequence of less uniform deposition; deposition during PS-PVD is a mix of solidification of liquid droplets,

condensation of individual adatoms, and condensation of nanoclusters, and is a less homogeneous process than EB-PVD.

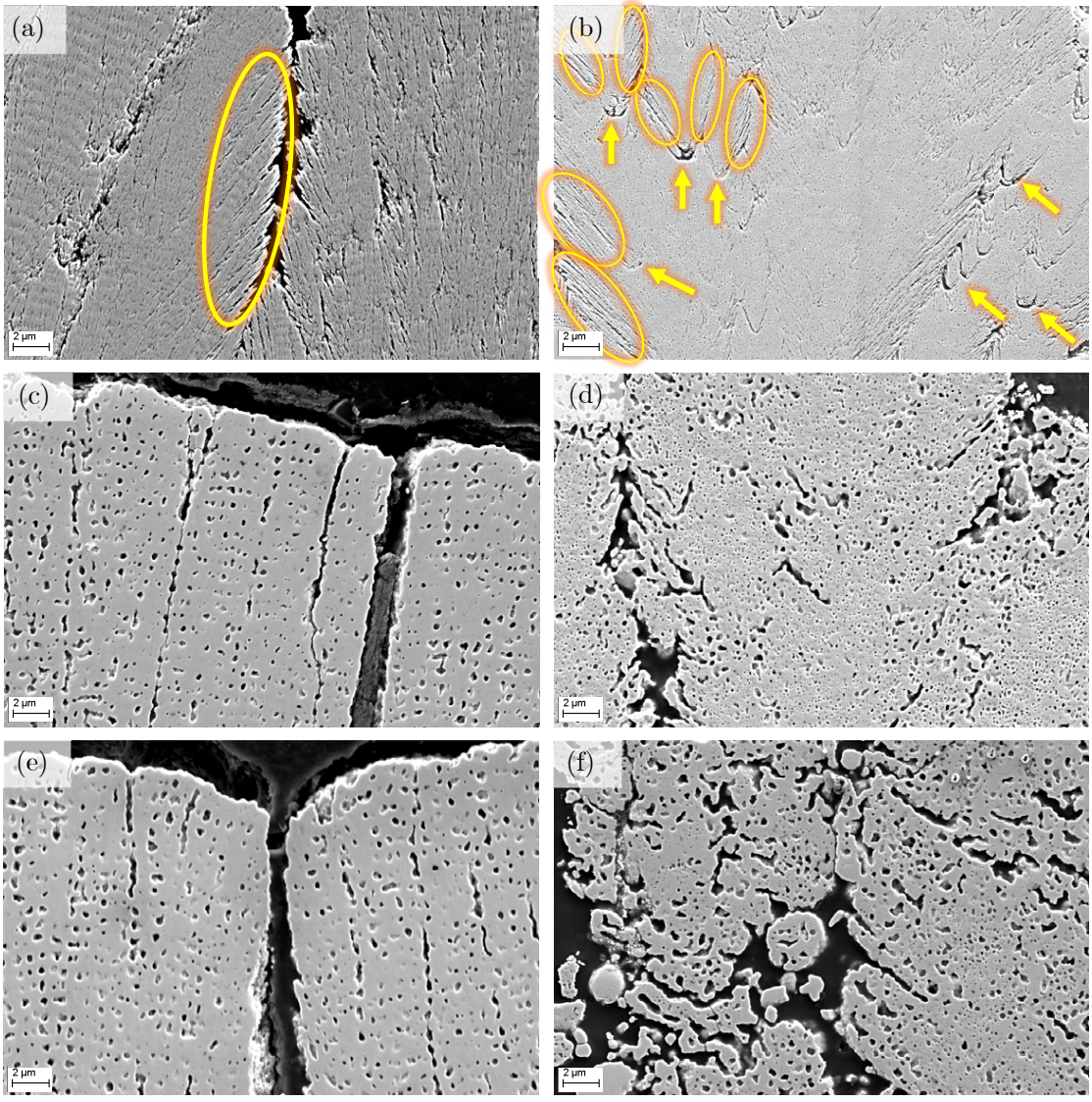

Figure 5.9: Cross-section SEM micrographs showing porosity of EB-PVD samples after 0 cycles (a), 300 cycles (c), and 600 cycles (e), and PS-PVD samples after 0 cycles (b), 300 cycles (d), and 600 cycles (f).

The featherlike morphology of the uncycled EB-PVD sample, an example of which is circled in Figure 5.9a, is the result of vapor-phase deposition [20]. In the EB-PVD process, high substrate temperature and low deposition rate result in high surface mobility of the depositing adatoms, which move by surface diffusion to minimize surface energy. The result is the growth of compact columns with preferred crystallographic texture [20, 52]. The PS-PVD uncycled sample has smaller subcolumns with featherlike branching, as circled in Figure 5.9b. The difference between the fairly straight, compact columns of EB-PVD coatings and the looser, highly branched, tapered columns of PS-PVD is illustrated in Figure 5.10, in which the edges of the columns have been highlighted with dashed lines.

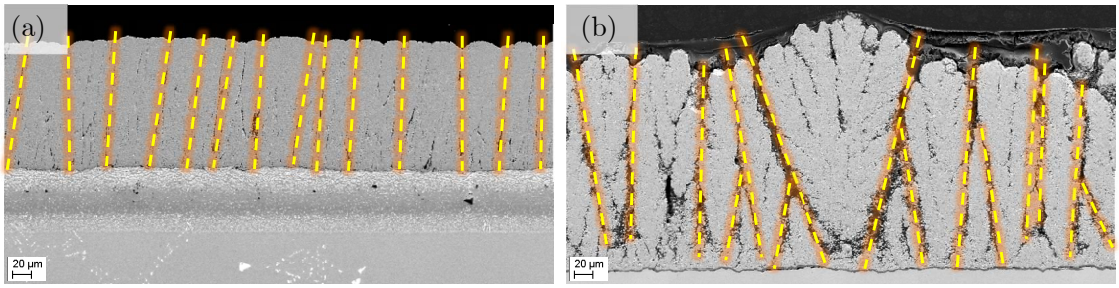

Figure 5.10: Cross-section SEM micrographs of an uncycled EB-PVD sample (a) and an uncycled PS-PVD sample (b). Dashed lines have been added to mark the column edges. The PS-PVD sample has tapered columns.

In the PS-PVD process, deposition of nanoclusters occurs, and these nanoclusters have lower mobility than individual adatoms and are less able to rearrange themselves to preserve the preferred crystallographic texture [20]. The nanoclusters are more likely to stick to the tips of taller columns and their lower mobility means that surface roughness cannot be smoothed, but rather intensifies as the coating grows. This "shadowing" effect results in tapered columns that are wider at the top of the coating with voids between them [23, 52] where slower-growing columns terminated upon reaching another column [23], as seen in Figure 5.10b. These nanoclusters, as well as partially melted particles, can serve as nucleation sites for new subcolumns, which then grow by

vapor-phase deposition of adatoms [20]. The concave U shapes marked with arrows in Figure 5.9b are likely nucleation sites of new subcolumns, and above them are the featherlike morphology of vapor-phase deposition (circled in Fig. 5.9b).

Bond Coat Phases and Diffusion of Substrate Elements

The expected as-deposited state for PtAl bond coats is a homogeneous top layer of β-(Ni,Pt)Al over an interdiffusion zone (IDZ) of β-phase with precipitates [117, 118]. While the uncycled PS-PVD sample, shown in Figure 5.11b, has the expected form, the uncycled EB-PVD sample has an unexpected two-phase region at the top of the bond coat, seen in Figure 5.11a. It is likely that the heat treatment given to the PS-PVD coatings allowed the bond coat to become homogeneous, as a homogenizing heat treatment is often done as a final step in the bond coat process [82, 117, 118]

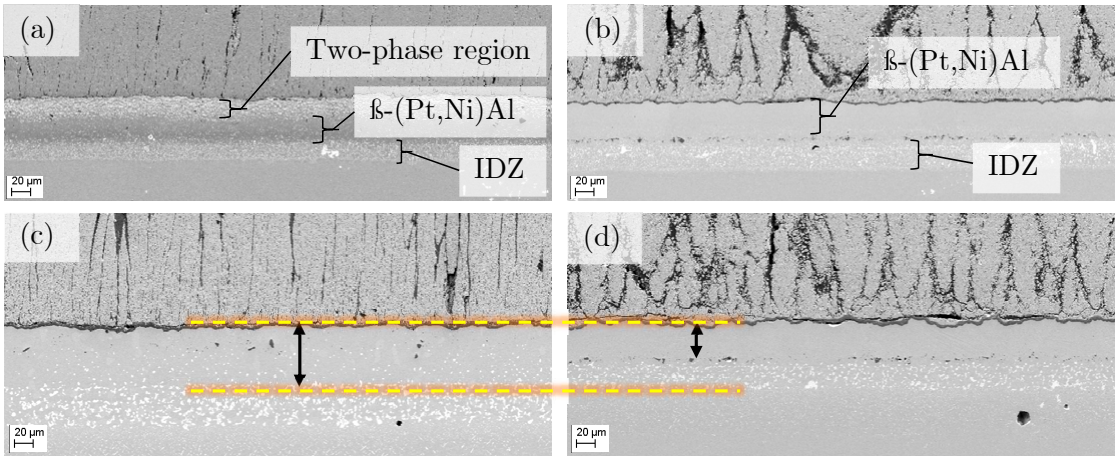

Figure 5.11: Cross-section SEM micrographs of EB-PVD samples after 0 cycles (a) and 300 cycles (c) and PS-PVD samples after 0 cycles (b) and 300 cycles (d), with the bond coat layers labeled in a and b and arrows showing the thickness of the β-phase layer in c and d.

After 300 thermal cycles, both the EB-PVD and PS-PVD samples had the expected β-phase layer over the IDZ, shown in Fig. 5.11c and d. The bond coat thickens over time as Ni diffuses from

substrate to bond coat faster than Al diffuses from bond coat to substrate and TGO [46]. After 300 cycles, the bond coat of the EB-PVD sample was significantly thicker than the bond coat of the PS-PVD sample, as indicated by the arrows in Fig. 5.11c and d, and the bond coat for the 600 cycle EB-PVD sample was also much thicker than that for PS-PVD, as shown in Figure 5.12a and b. Though only one sample of each combination of coating type and thermal history was sectioned for microscopy and there is statistical variation in bond coat thickness among samples, this does indicate that diffusion in the bond coat occurred faster in the EB-PVD samples than in the PS-PVD samples.

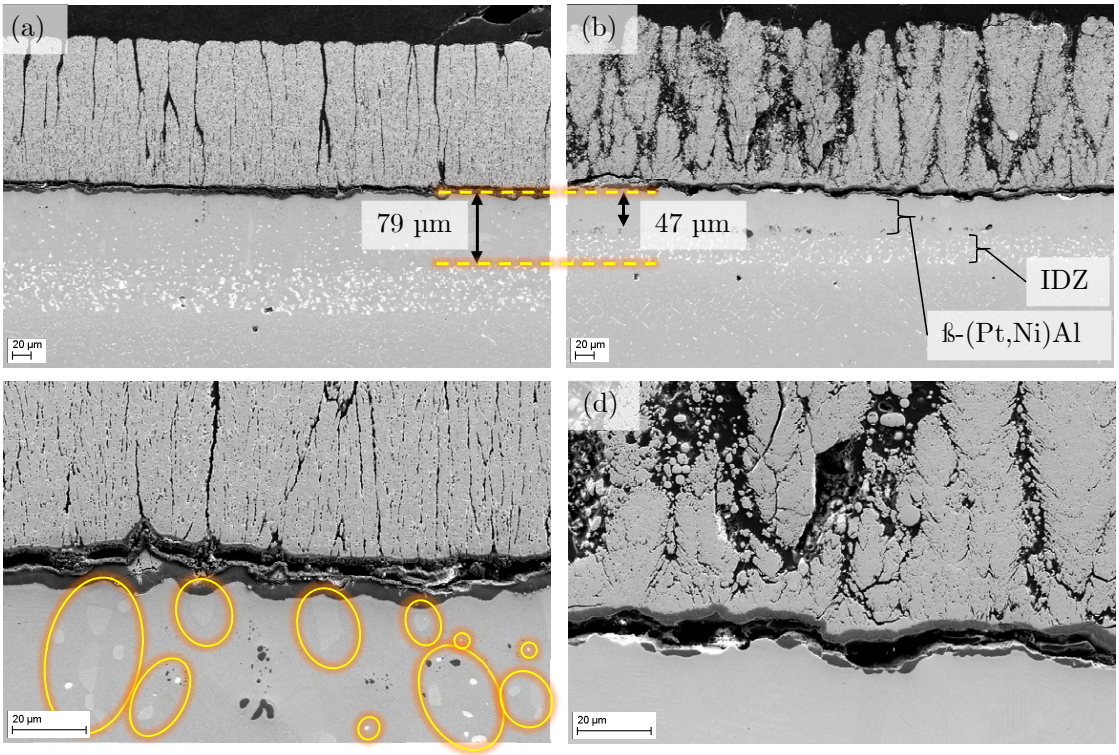

Figure 5.12: Cross-section SEM micrographs of an EB-PVD sample (a and c) and a PS-PVD sample (b and d) after 600 thermal cycles at two magnifications. The EB-PVD has a thicker bond coat (indicated with arrows in a and b) and has more precipitates and other phases closer to the TGO (circled in c).

Closer views of these samples are shown in Figure 5.12. The bond coat of the EB-PVD sample

(shown in Fig. 5.12a and c) is much thicker than that of the PS-PVD sample (shown in Fig. 5.12b and d), as indicated with arrows. Non-matrix phases have reached the TGO for the EB-PVD sample (examples circled in Fig. 5.12c) but not for the PS-PVD sample (Fig. 5.12d), indicating that substrate elements have diffused through the bond coat faster for the EB-PVD sample. While the heat treatment given to the PS-PVD samples and not the EB-PVD samples is likely the cause of the different bond coat microstructures for the two coating types, it is not expected that this would be the reason for the apparently faster diffusion in the bond coats of the EB-PVD samples after thermal cycling. One additional hour of thermal exposure is not likely to make a difference when both coating types have had hundreds of thermal cycles. A possibility is that inhomogeneous heat distribution inside the furnace used for thermal cycling caused some samples to be thermally cycled at a higher temperature than others, as the positions of the samples were not rotated during cycling. If the EB-PVD samples were cycled at a slightly higher temperature than the PS-PVD samples, this could cause faster diffusion of substrate elements.

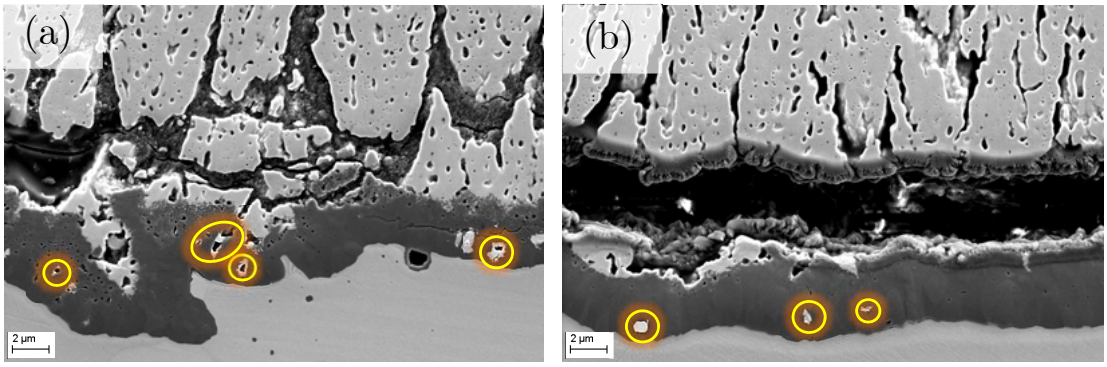

Figure 5.13: Cross-section SEM micrographs of an EB-PVD sample after 300 cycles (a) and 600 cycles (b) showing bright inclusions in the TGO.

Small bright inclusions were observed in the TGO of the EB-PVD samples but not the PS-PVD samples; this is undesirable, as additional elements in the TGO degrade adherence by serving as sites of stress concentration and causing additional thermal expansion mismatch stresses during

thermal cycling, and degrade oxidation resistance by serving as paths of faster oxygen transport than the surrounding α-alumina [121]. The inclusions appear to form inside pores in the TGO, as pores are visible inside the inclusions in the 300 cycle sample but not the 600 cycle sample, implying by this time the pores have been filled.

Conclusions

The findings drawn from the SEM and EDS investigations are summarized below.

- Greater TGO convolution and more extensive cracking and delamination with increased thermal cycling was observed for both coating types, supporting the conclusion that both TGO lengthening and damage accumulation were responsible for the reduction of TGO compressive stress reported in Chapter 4.
- The PS-PVD samples had much greater convolution of the TGO than did the EB-PVD samples of the same thermal history. This is possibly due to the interface being rougher in the as-deposited state or to the higher degree of defects and voids in the YSZ.
- While both coating types had extensive cracking and delamination after thermal cycling, the crack paths were different. The EB-PVD coatings had cracking and delaminations along the TGO/YSZ interface, whereas the PS-PVD coatings had substantial cracking within and across the TGO and through the YSZ, "jumping" from crest to crest. The greater degree of convolution for the PS-PVD TGO can serve as crack initiation sites on the flanks of the crests, and would also be more difficult for cracks to follow, diverting cracks into the YSZ or across the TGO.
- The greater extent of voids and gaps in the YSZ near the TGO for the PS-PVD samples make the YSZ less resistant to cracking compared to the denser YSZ morphology in the EB-

PVD samples. Some of these voids contained unmelted particles, likely the source of the monoclinic zirconia phase detected in Chapter 4; as the monoclinic phase has lower fracture toughness, this would also reduce resistance to cracking. These factors likely contributed to the greater extent of cracking in the YSZ for the PS-PVD samples compared to the EB-PVD samples.

- The TGO of the PS-PVD samples had a greater fraction of porous intermixed zone relative to fully dense zone compared to the EB-PVD samples, and had frequent cracking within and across the intermixed zone as well as between the two TGO zones. This may be due to the PS-PVD samples having more voids at the YSZ/TGO interface. The greater extent of cracking within the TGO itself rather than along the interface may be the reason for the lower TGO stress for the PS-PVD samples that was reported in Chapter 4.

- Evidence for different deposition mechanisms for the two coating types was observed. The uncycled EB-PVD sample had the compact columnar structure with featherlike column edges that indicates vapor-phase deposition. The uncycled PS-PVD sample had tapered columns with small-scale vapor deposition in the subcolumns on nanocluster nucleation sites.

- While the PS-PVD uncycled sample had the expected β-phase layer and interdiffusion zone, the EB-PVD uncycled sample had a two-phase layer at the top of the bond coat. It is likely that the heat treatment given to the PS-PVD samples served to homogenize this two-phase region.

- The cycled EB-PVD samples had a thicker bond coat than PS-PVD and had larger precipitate phases that had reached the TGO, while the precipitate phases in the PS-PVD samples did not extend beyond the IDZ. The EB-PVD samples also had inclusions in the TGO, while the PS-PVD samples did not. These observations indicate that diffusion of substrate elements

occurred faster for the EB-PVD samples, which is undesirable because these elements in the TGO and at the TGO/BC interface degrade adherence and oxidation protection.

CHAPTER 6: CONCLUSIONS

This work investigated the residual stress evolution and damage modes in thermally cycled TBCs manufactured by PS-PVD, an attractive developing deposition technology. Coatings manufactured by the industry standard EB-PVD process and thermally cycled in the same way were also investigated to serve as a baseline for comparison. Samples were thermally cycled for 0, 300, or 600 thermal cycles to simulate new, mid-life, and near-end-of-life coatigns. Stresses were measured by nondestructive spectroscopy methods while cracking and damage modes were investigated by scanning electron microscopy and energy dispersive X-ray spectroscopy.

In Chapter 4 the results of the stress investigations were reported. Residual stress in the YSZ topcoat is of interest because it drives cracking that can lead to spallation failure by coalescence of cracks. Raman spectroscopy was used for these stress measurements as well as phase identification. The undesirable monoclinic zirconia phase was found in all PS-PVD samples and no EB-PVD samples, as well as the powder used in the PS-PVD deposition process. The presence of monoclinic phase in the PS-PVD coatings is due to incompletely melted powder particles. This phase has lower fracture toughness than the dominant tetragonal phase, providing a lower barrier to cracking within the topcoat.

The uncycled PS-PVD topcoats were in mild compression, in contrast to the tensile state reported in the literature for uncycled PS-PVD coatings. This difference is attributed to the one hour heat treatment that was applied to the coatings to restore oxygen to the coatings; other works in the literature did not require this heat treatment because additional oxygen was supplied during coating deposition. The uncycled EB-PVD had moderately tensile stress, which was more tensile than expected but not unprecedented based on the literature [64]. This may be due to the highly localized nature of the Raman measurements, as the spot size is smaller than an individual column. Both

topcoat types became more compressive with thermal cycling, which was expected due to sintering, and had stresses of about 175–250 MPa compressive after 300 cycles and about 300–350 MPa compressive after 600 cycles. These values are in the range expected from the literature [22, 105].

Photoluminescence piezospectroscopy was used to quantify residual stress in the TGO, which is an important indicator of damage and lifetime. The stress in the TGO was bimodal for all samples due to the fluorescing volume containing both intact and cracked TGO. The uncycled EB-PVD samples did not have sufficient TGO thickness to produce stress maps, while the PS-PVD samples did thanks to the one hour heat treatment they received. The TGO stress in the uncycled PS-PVD samples was around 4 GPa for the more-stressed state (representing intact TGO), in the expected range from the literature. This stress was relieved by about 1.5 GPa between 0 and 300 thermal cycles due to both the TGO lengthening as it became more convoluted and due to microcracking and local damage. Both coating types had similar TGO stress after 300 cycles, around 2.5 GPa compressive for the higher-stressed doublet, and was relieved further to around 2 GPa compressive for both coating types after 600 cycles. The PS-PVD samples had slightly greater stress relief and slightly lower stress after 600 cycles than did EB-PVD, but the values were still quite similar for the two coating types.

Chapter 5 reported the results of investigations into microstructural evolution and damage modes by scanning electron microscopy and energy dispersive X-ray spectroscopy. With increased thermal cycling both coating types had increasing convolution of the TGO and more extensive cracking and delamination, supporting the conclusion in Chapter 4 that both TGO lengthening and local damage were responsible for the measured stress relief in the TGO. For coatings of the same thermal history the PS-PVD coatings had greater TGO convolution than the EB-PVD coatings, which is possibly due to the PS-PVD topcoat having more voids and defects than EB-PVD or the as-coated interface being rougher.

While cracking and delamination were extensive after thermal cycling for both coating types, a much greater fraction of the cracks in the PS-PVD samples crossed the TGO, as opposed to most of the cracking in the EB-PVD samples occurring along the TGO/YSZ interface. This is the likely reason for the slightly lower TGO stress for PS-PVD coatings that was reported in Chapter 4. The EB-PVD samples' delaminations and cracks being almost entirely along the interface was likely due in part to the much flatter interface, whereas the more highly convoluted interface in the PS-PVD samples diverted the cracks into the YSZ above the TGO. There was also less resistance to cracking in the YSZ in PS-PVD coatings due to the greater extent of defects and voids, as well as unmelted particles that were the probably source of the monoclinic phase reported in Chapter 4. The greater extent of voids in the YSZ near the interface for the PS-PVD samples is likely a contributor to the greater fraction of porous intermixed zone in the TGO relative to the fully dense alumina zone. In turn, the greater fraction of porous intermixed zone in the TGO of the PS-PVD samples is probably the reason for the greater extent of cracking within the TGO rather than along the interface as for EB-PVD.

The uncycled EB-PVD samples had a marbled two-phase layer at the top of the bond coat, under which was the expected layer of β-phase with precipitates and interdiffusion zone. The uncycled PS-PVD samples, in contrast, had only the expected homogeneous β-phase and IDZ. This is likely because the heat treatment given to the PS-PVD samples homogenized the two-phase region. After thermal cycling, the bond coat of the EB-PVD samples was thicker than that of the PS-PVD samples and the non-matrix phases were larger and much closer to the TGO; there were also inclusions in the TGO for the EB-PVD samples but not the PS-PVD. These observations indicate that diffusion of substrate elements through the bond coat toward the TGO occurred faster for the EB-PVD coatings, which is undesirable as these elements and phases degrade coating adherence and degrade the oxidation protection of the bond coat and TGO. The mechanism by which the top coat could affect the rate of diffusion through the bond coat is not apparent, and a possible reason

for this difference is inhomogeneous heating in the furnace during thermal cycling.

Despite the different stress states between the two coating types for the uncycled samples, the similar stress evolution and stress after cycling is a promising indicator that PS-PVD has satisfactory lifetime and resistance to damage compared to EB-PVD, and may be a viable alternative deposition process. None of the testing coatings experienced visible spallation, even after 600 thermal cycles.

The ability to tailor the microstructure of PS-PVD coatings by adjusting the processing parameters makes this deposition process an exciting new avenue of coating development. Tuning the processing parameters, such as plasma power and chamber pressure, to achieve more complete vaporization of the feedstock may produce more homogeneous coatings with microstructure and crack modes more like the strain-tolerant EB-PVD coatings. The ability of PS-PVD to coat much more complex part geometries will enable designers to take full advantage of such other innovations as additively manufactured engine components with features such as internal cooling structures more complex than is currently available. The results of this work evaluating the performance and lifetime of PS-PVD TBCs contributes to the body of knowledge necessary for PS-PVD to reach its potential as an innovative and valuable deposition technique.

APPENDIX A: CONVERSION OF XRD STRAIN TO STRESS

Strain values found in X-ray diffraction may be converted to stress using Equation A.1 [122]:

$$\sigma_{22} = \frac{1}{b}\Big(\varepsilon_{22} - \frac{a(\varepsilon_{11} + \varepsilon_{22} + \varepsilon_{33})}{3a + b}\Big) \tag{A.1}$$

where a and b are the X-ray elastic constants (XECs). In this work the XECs used, reported in Table A.1, were calculated using the DECcalc software using the stiffness constants in Table A.2 [2] and the Eshelby-Kröner method.

Table A.1: X-ray elastic constants (XECs) calculated with stiffness constants using DECcalc software.

Lattice plane	$a = S_1$ (GPa^{-1})	$b = \frac{1}{2}S_2$ (GPa^{-1})
(116)	-6.16×10^{-7}	3.22×10^{-6}
(024)	-5.58×10^{-7}	3.03×10^{-6}

Table A.2: Stiffness constants for α-alumina [2] used to determine X-ray constants.

C_{ij}	Stiffness (GPa)
C_{11}	479
C_{33}	477
C_{44}	147
C_{12}	154
C_{13}	118
C_{14}	-19

In this work, ε_{11} and ε_{22} are the strains in the two in-plane directions and ε_{33} is the out-of-plane strain. Assuming that the stresses in the in-plane directions are equal ($\varepsilon_{11} = \varepsilon_{22}$), Equation A.1 becomes Equation A.2:

$$\sigma_{22} = \frac{1}{b}\Big(\varepsilon_{22} - \frac{a(\varepsilon_{33} + 2\varepsilon_{22})}{3a + b}\Big) \tag{A.2}$$

The TGO strain results at room temperature found in [56] were converted to stress using Equation A.2.

LIST OF REFERENCES

[1] He, J. and Clarke, D. R., "Determination of the piezospectroscopic coefficients for chromium-doped sapphire," *Journal of the American Ceramic Society*, Vol. 78, No. 5, 1995, pp. 1347–1353.

[2] Shang, S.-L., Zhang, H., Wang, Y., and Liu, Z.-K., "Temperature-dependent elastic stiffness constants of α-and θ-Al2O3 from first-principles calculations," *Journal of Physics: Condensed Matter*, Vol. 22, No. 37, 2010, pp. 375403.

[3] Miller, R. A., "Current status of thermal barrier coatings—an overview," *Surface and Coatings Technology*, Vol. 30, No. 1, 1987, pp. 1–11.

[4] Padture, N. P., Gell, M., and Jordan, E. H., "Thermal barrier coatings for gas-turbine engine applications," *Science*, Vol. 296, No. 5566, 2002, pp. 280–284.

[5] Clarke, D. R., Oechsner, M., and Padture, N. P., "Thermal-barrier coatings for more efficient gas-turbine engines," *MRS bulletin*, Vol. 37, No. 10, 2012, pp. 891–898.

[6] Li, C., Zhang, X., Chen, Y., Carr, J., Jacques, S., Behnsen, J., di Michiel, M., Xiao, P., and Cernik, R., "Understanding the residual stress distribution through the thickness of atmosphere plasma sprayed (APS) thermal barrier coatings (TBCs) by high energy synchrotron XRD; digital image correlation (DIC) and image based modelling," *Acta Materialia*, Vol. 132, 2017, pp. 1 – 12.

[7] Harder, B. J. and Zhu, D., "Plasma spray-physical vapor deposition (PS-PVD) of ceramics for protective coatings," *NASA Technical Reports*, 2011.

[8] Cernuschi, F., Lorenzoni, L., Capelli, S., Guardamagna, C., Karger, M., Vaßen, R., Von Niessen, K., Markocsan, N., Menuey, J., and Giolli, C., "Solid particle erosion of

thermal spray and physical vapour deposition thermal barrier coatings," *Wear*, Vol. 271, No. 11-12, 2011, pp. 2909–2918.

[9] Wen, M., Jordan, E. H., and Gell, M., "Analysis of localized damage in EB-PVD/(Ni, Pt) Al thermal barrier coatings," *Surface and Coatings Technology*, Vol. 200, No. 18-19, 2006, pp. 5193–5202.

[10] Miller, R. A., "Thermal barrier coatings for aircraft engines: history and directions," *Journal of thermal spray technology*, Vol. 6, No. 1, 1997, pp. 35.

[11] Evans, A. G., Mumm, D., Hutchinson, J., Meier, G., and Pettit, F., "Mechanisms controlling the durability of thermal barrier coatings," *Progress in materials science*, Vol. 46, No. 5, 2001, pp. 505–553.

[12] Rezanka, S., Mauer, G., and Vaßen, R., "Improved thermal cycling durability of thermal barrier coatings manufactured by PS-PVD," *Journal of Thermal Spray Technology*, Vol. 23, No. 1-2, 2014, pp. 182–189.

[13] Ren, X., Zhao, M., Feng, J., and Pan, W., "Phase transformation behavior in air plasma sprayed yttria stabilized zirconia coating," *Journal of Alloys and Compounds*, Vol. 750, 2018, pp. 189–196.

[14] Harder, B. J., Zhu, D., Schmitt, M. P., and Wolfe, D. E., "Microstructural Effects and Properties of Non-line-of-Sight Coating Processing via Plasma Spray-Physical Vapor Deposition," *Journal of Thermal Spray Technology*, Vol. 26, No. 6, 2017, pp. 1052–1061.

[15] Manero II, A., Selimov, A., Fouliard, Q., Knipe, K., Wischek, J., Meid, C., Karlsson, A. M., Bartsch, M., and Raghavan, S., "Piezospectroscopic evaluation and damage identification for thermal barrier coatings subjected to simulated engine environments," *Surface and Coatings Technology*, Vol. 323, 2017, pp. 30–38.

[16] Von Niessen, K., Gindrat, M., and Refke, A., "Vapor phase deposition using plasma spray-PVD," *Journal of thermal spray technology*, Vol. 19, No. 1-2, 2010, pp. 502–509.

[17] Mauer, G., Hospach, A., and Vaßen, R., "Process development and coating characteristics of plasma spray-PVD," *Surface and Coatings Technology*, Vol. 220, 2013, pp. 219–224.

[18] Rezanka, S., Mack, D. E., Mauer, G., Sebold, D., Guillon, O., and Vaßen, R., "Investigation of the resistance of open-column-structured PS-PVD TBCs to erosive and high-temperature corrosive attack," *Surface and Coatings Technology*, Vol. 324, 2017, pp. 222–235.

[19] Smith, M. F., Hall, A. C., Fleetwood, J. D., and Meyer, P., "Very low pressure plasma spray—a review of an emerging technology in the thermal spray community," *Coatings*, Vol. 1, No. 2, 2011, pp. 117–132.

[20] Rezanka, S., Somsen, C., Eggeler, G., Mauer, G., Vaßen, R., and Guillon, O., "A TEM Investigation of Columnar-Structured Thermal Barrier Coatings Deposited by Plasma Spray-Physical Vapor Deposition (PS-PVD)," *Plasma Chemistry and Plasma Processing*, 2018, pp. 1–12.

[21] He, W., Mauer, G., Schwedt, A., Guillon, O., and Vaßen, R., "Advanced crystallographic study of the columnar growth of YZS coatings produced by PS-PVD," *Journal of the European Ceramic Society*, Vol. 38, No. 5, 2018, pp. 2449–2453.

[22] Yang, J., Zhao, H., Zhong, X., Ni, J., Zhuang, Y., Wang, L., and Tao, S., "Evolution of Residual Stresses in PS-PVD Thermal Barrier Coatings on Thermal Cycling," *Journal of Thermal Spray Technology*, 2018, pp. 1–10.

[23] Shao, F., Zhao, H., Zhong, X., Zhuang, Y., Cheng, Z., Wang, L., and Tao, S., "Characteristics of thick columnar YSZ coatings fabricated by plasma spray-physical vapor deposition," *Journal of the European Ceramic Society*, Vol. 38, No. 4, 2018, pp. 1930–1937.

[24] Young, E. J., Mateeva, E., Moore, J. J., Mishra, B., and Loch, M., "Low pressure plasma spray coatings," *Thin Solid Films*, Vol. 377, 2000, pp. 788–792.

[25] Hospach, A., Mauer, G., Vaßen, R., and Stöver, D., "Columnar-structured thermal barrier coatings (TBCs) by thin film low-pressure plasma spraying (LPPS-TF)," *Journal of thermal spray technology*, Vol. 20, No. 1-2, 2011, pp. 116–120.

[26] Sampath, S., Schulz, U., Jarligo, M. O., and Kuroda, S., "Processing science of advanced thermal-barrier systems," *MRS bulletin*, Vol. 37, No. 10, 2012, pp. 903–910.

[27] Lv, B., Mücke, R., Fan, X., Wang, T., Guillon, O., and Vaßen, R., "Sintering resistance of advanced plasma-sprayed thermal barrier coatings with strain-tolerant microstructures," *Journal of the European Ceramic Society*, Vol. 38, No. 15, 2018, pp. 5092–5100.

[28] Gell, M., Xie, L., Ma, X., Jordan, E. H., and Padture, N. P., "Highly durable thermal barrier coatings made by the solution precursor plasma spray process," *Surface and Coatings Technology*, Vol. 177, 2004, pp. 97–102.

[29] Padture, N., Schlichting, K., Bhatia, T., Ozturk, A., Cetegen, B., Jordan, E., Gell, M., Jiang, S., Xiao, T., Strutt, P., et al., "Towards durable thermal barrier coatings with novel microstructures deposited by solution-precursor plasma spray," *Acta materialia*, Vol. 49, No. 12, 2001, pp. 2251–2257.

[30] Martena, M., Botto, D., Fino, P., Sabbadini, S., Gola, M., and Badini, C., "Modelling of TBC system failure: Stress distribution as a function of TGO thickness and thermal expansion mismatch," *Engineering Failure Analysis*, Vol. 13, No. 3, 2006, pp. 409–426.

[31] Von Niessen, K. and Gindrat, M., "Plasma spray-PVD: a new thermal spray process to deposit out of the vapor phase," *Journal of thermal spray technology*, Vol. 20, No. 4, 2011, pp. 736–743.

[32] Schulz, U., "Phase transformation in EB-PVD yttria partially stabilized zirconia thermal barrier coatings during annealing," *Journal of the American Ceramic Society*, Vol. 83, No. 4, 2000, pp. 904–910.

[33] Schmitt, M. P., Harder, B. J., and Wolfe, D. E., "Process-structure-property relations for the erosion durability of plasma spray-physical vapor deposition (PS-PVD) thermal barrier coatings," *Surface and Coatings Technology*, Vol. 297, 2016, pp. 11–18.

[34] Spinhirne, N. R., *The development and characterization of novel yttria-stabilized zirconia coatings deposited by very low pressure plasma spray*, Ph.D. thesis, New Mexico Institute of Mining and Technology, 2008.

[35] He, W., Mauer, G., Gindrat, M., Wäger, R., and Vaßen, R., "Investigations on the nature of ceramic deposits in plasma spray–physical vapor deposition," *Journal of Thermal Spray Technology*, Vol. 26, No. 1-2, 2017, pp. 83–92.

[36] Rossmann, L., Northam, M., Sarley, B., Chernova, L., Viswanathan, V., Harder, B., and Raghavan, S., "Investigation of TGO stress in thermally cycled plasma-spray physical vapor deposition and electron-beam physical vapor deposition thermal barrier coatings via photoluminescence spectroscopy," *Surface and Coatings Technology*, 2019, (submitted).

[37] Gell, M., Duhl, D., Gupta, D., and Sheffler, K., "Advanced superalloy airfoils," *JOM*, Vol. 39, No. 7, 1987, pp. 11–15.

[38] Tolpygo, V., Clarke, D., and Murphy, K., "The effect of grit blasting on the oxidation behavior of a platinum-modified nickel-aluminide coating," *Metallurgical and materials transactions A*, Vol. 32, No. 6, 2001, pp. 1467–1478.

[39] Hasselman, D., Johnson, L. F., Bentsen, L. D., SYED, R., LEE, H. L., and SWAIN, M. V.,

"Thermal Diffusivity and Conductivity of Dense Polycrystalline Zr0," *Am. Ceram. Soc. Bull*, Vol. 66, No. 5, 1987, pp. 799–806.

[40] Azzopardi, A., Mévrel, R., Saint-Ramond, B., Olson, E., and Stiller, K., "Influence of aging on structure and thermal conductivity of Y-PSZ and Y-FSZ EB-PVD coatings," *Surface and coatings technology*, Vol. 177, 2004, pp. 131–139.

[41] Schulz, U., Fritscher, K., Leyens, C., and Peters, M., "High-Temperature Aging of EB-PVD Thermal Barrier Coating," *CESP*, Vol. 12, No. 4, 2001, pp. 347–356.

[42] Moon, J., Choi, H., Kim, H., and Lee, C., "The effects of heat treatment on the phase transformation behavior of plasma-sprayed stabilized ZrO2 coatings," *Surface and Coatings Technology*, Vol. 155, No. 1, 2002, pp. 1–10.

[43] Schulz, U., Saruhan, B., Fritscher, K., and Leyens, C., "Review on Advanced EB-PVD Ceramic Topcoats for TBC Applications," *International journal of applied ceramic technology*, Vol. 1, No. 4, 2004, pp. 302–315.

[44] Smialek, J. L., Harder, B. J., and Garg, A., "Oxidative durability of TBCs on Ti2AlC MAX phase substrates," *Surface and Coatings Technology*, Vol. 285, 2016, pp. 77–86.

[45] Sohn, Y., Vaidyanathan, K., Ronski, M., Jordan, E., and Gell, M., "Thermal cycling of EB-PVD/MCrAlY thermal barrier coatings: II. Evolution of photo-stimulated luminescence," *Surface and Coatings Technology*, Vol. 146, 2001, pp. 102–109.

[46] Heeg, B., Tolpygo, V. K., and Clarke, D. R., "Damage evolution in thermal barrier coatings with thermal cycling," *Journal of the American Ceramic Society*, Vol. 94, 2011, pp. s112–s119.

[47] Sridharan, S., Xie, L., Jordan, E. H., and Gell, M., "Stress variation with thermal cycling in

the thermally grown oxide of an EB-PVD thermal barrier coating," *Surface and Coatings Technology*, Vol. 179, No. 2-3, 2004, pp. 286–296.

[48] Gell, M., Jordan, E., Vaidyanathan, K., McCarron, K., Barber, B., Sohn, Y.-H., and Tolpygo, V. K., "Bond strength, bond stress and spallation mechanisms of thermal barrier coatings," *Surface and Coatings Technology*, Vol. 120, 1999, pp. 53–60.

[49] Chen, Q.-Y., Li, C.-X., Zhao, J.-Z., Yang, G.-J., and Li, C.-J., "Microstructure of YSZ coatings deposited by PS-PVD using 45 kW shrouded plasma torch," *Materials and Manufacturing Processes*, Vol. 31, No. 9, 2016, pp. 1183–1191.

[50] Goral, M., Kotowski, S., Nowotnik, A., Pytel, M., Drajewicz, M., and Sieniawski, J., "PS-PVD deposition of thermal barrier coatings," *Surface and Coatings Technology*, Vol. 237, 2013, pp. 51–55.

[51] Gao, L., Wei, L., Guo, H., Gong, S., and Xu, H., "Deposition mechanisms of yttria-stabilized zirconia coatings during plasma spray physical vapor deposition," *Ceramics International*, Vol. 42, No. 4, 2016, pp. 5530–5536.

[52] Mauer, G., Hospach, A., Zotov, N., and Vaßen, R., "Process conditions and microstructures of ceramic coatings by gas phase deposition based on plasma spraying," *Journal of thermal spray technology*, Vol. 22, No. 2-3, 2013, pp. 83–89.

[53] Gao, L., Guo, H., Wei, L., Li, C., Gong, S., and Xu, H., "Microstructure and mechanical properties of yttria stabilized zirconia coatings prepared by plasma spray physical vapor deposition," *Ceramics International*, Vol. 41, No. 7, 2015, pp. 8305–8311.

[54] Minerals, Metals & Materials Society, "Compositions of Typical Cast Superalloys," webpage.

[55] Weyant, C., Almer, J., and Faber, K., "Through-thickness determination of phase composition and residual stresses in thermal barrier coatings using high-energy X-rays," *Acta materialia*, Vol. 58, No. 3, 2010, pp. 943–951.

[56] Northam, M., Rossmann, L., Sarley, B., Harder, B., Park, J., Kenesei, P., Almer, J., Viswanathan, V., and Raghavan, S., "Comparison of electron-beam physical vapor deposition and plasma-spray physical vapor deposition thermal barrier coating properties using synchrotron X-ray diffraction," *Proceedings of the ASME 2019 Turbomachinery Technical Conference & Exposition*, June 2019.

[57] Nanophoton, "Basics of Raman Spectroscopy," .

[58] Princeton Instruments, "Raman Spectroscopy Basics," .

[59] Umbach, "Fundamentals of Raman Spectroscopy," website of Laser Spectroscopy Labs, UC Irvine.

[60] Lughi, V. and Clarke, D. R., "Transformation of Electron-Beam Physical Vapor-Deposited 8 wt% Yttria-Stabilized Zirconia Thermal Barrier Coatings," *Journal of the American Ceramic Society*, Vol. 88, No. 9, 2005, pp. 2552–2558.

[61] Limarga, A. M., Iveland, J., Gentleman, M., Lipkin, D. M., and Clarke, D. R., "The use of Larson–Miller parameters to monitor the evolution of Raman lines of tetragonal zirconia with high temperature aging," *Acta Materialia*, Vol. 59, No. 3, 2011, pp. 1162–1167.

[62] Sekulic, A., Furic, K., Tonejc, A., Tonejc, A., and Stubicar, M., "Determination of the monoclinic, tetragonal and cubic phases in mechanically alloyed ZrO2-Y2O3 and ZrO2-CoO powder mixtures by Raman spectroscopy," *Journal of materials science letters*, Vol. 16, No. 4, 1997, pp. 260–262.

[63] Atkinson, A. and Jain, S., "Spatially resolved stress analysis using Raman spectroscopy," *Journal of Raman spectroscopy*, Vol. 30, No. 10, 1999, pp. 885–891.

[64] Tomimatsu, T., Kagawa, Y., and Zhu, S., "Residual stress distribution in electron beam-physical vapor deposited ZrO 2 thermal barrier coating layer by raman spectroscopy," *Metallurgical and Materials Transactions A*, Vol. 34, No. 8, 2003, pp. 1739–1741.

[65] Krämer, S., Faulhaber, S., Chambers, M., Clarke, D., Levi, C., Hutchinson, J., and Evans, A., "Mechanisms of cracking and delamination within thick thermal barrier systems in aero-engines subject to calcium-magnesium-alumino-silicate (CMAS) penetration," *Materials Science and Engineering: A*, Vol. 490, No. 1-2, 2008, pp. 26–35.

[66] Tanaka, M., Kitazawa, R., Tomimatsu, T., Liu, Y., and Kagawa, Y., "Residual stress measurement of an EB-PVD Y2O3-ZrO2 thermal barrier coating by micro-Raman spectroscopy," *Surface and Coatings Technology*, Vol. 204, No. 5, 2009, pp. 657–660.

[67] Tanaka, M., Hasegawa, M., Dericioglu, A., and Kagawa, Y., "Measurement of residual stress in air plasma-sprayed Y2O3–ZrO2 thermal barrier coating system using micro-Raman spectroscopy," *Materials Science and Engineering: A*, Vol. 419, No. 1-2, 2006, pp. 262–268.

[68] Garces, H. F., Senturk, B. S., and Padture, N. P., "In situ Raman spectroscopy studies of high-temperature degradation of thermal barrier coatings by molten silicate deposits," *Scripta Materialia*, Vol. 76, 2014, pp. 29–32.

[69] Mao, W., Chen, Q., Dai, C., Yang, L., Zhou, Y., and Lu, C., "Effects of piezo-spectroscopic coefficients of 8 wt.% Y2O3 stabilized ZrO2 on residual stress measurement of thermal barrier coatings by Raman spectroscopy," *Surface and Coatings Technology*, Vol. 204, No. 21-22, 2010, pp. 3573–3577.

[70] Syassen, K., "Ruby under pressure," *High Pressure Research*, Vol. 28, No. 2, 2008, pp. 75–126.

[71] Momma, K. and Izumi, F., "VESTA 3 for three-dimensional visualization of crystal, volumetric and morphology data," *J. Appl. Crystallogr.*, Vol. 44, 2011, pp. 1272–1276.

[72] Ma, Q. and Clarke, D. R., "Piezospectroscopic determination of residual stresses in polycrystalline alumina," *Journal of the American Ceramic Society*, Vol. 77, No. 2, 1994, pp. 298–302.

[73] Christensen, R., Lipkin, D., Clarke, D. R., and Murphy, K., "Nondestructive evaluation of the oxidation stresses through thermal barrier coatings using Cr3+ piezospectroscopy," *Applied Physics Letters*, Vol. 69, No. 24, 1996, pp. 3754–3756.

[74] Lipkin, D., , and Clarke, D., "Measurement of the stress in oxide scales formed by oxidation of alumina-forming alloys," *Oxidation of Metals*, Vol. 45, No. 3-4, 1996, pp. 267–280.

[75] Xu, Z., Wang, Z., Huang, G., Mu, R., and He, L., "Thermal cycling behavior of EB-PVD TBCs on CVD platinum modified aluminide coatings," *Journal of Alloys and Compounds*, Vol. 637, 2015, pp. 226–233.

[76] Lipkin, D., Schaffer, H., Adar, F., and Clarke, D., "Lateral growth kinetics of α-alumina accompanying the formation of a protective scale on (111) NiAl during oxidation at 1100 C," *Applied Physics Letters*, Vol. 70, No. 19, 1997, pp. 2550–2552.

[77] Clarke, D. R., Tolpygo, V., and Gentleman, M., "Luminescence-based characterization of protective oxides: from failure mechanisms to non-destructive evaluation," *Materials Science Forum*, Vol. 461, Trans Tech Publ, 2004, pp. 621–630.

[78] Nychka, J. and Clarke, D., "Damage quantification in TBCs by photo-stimulated luminescence spectroscopy," *Surface and Coatings Technology*, Vol. 146, 2001, pp. 110–116.

[79] Michaels, C. A. and Cook, R. F., "Determination of residual stress distributions in polycrystalline alumina using fluorescence microscopy," *Materials & Design*, Vol. 107, 2016, pp. 478 – 490.

[80] Selcuk, A. and Atkinson, A., "Analysis of the Cr3+ luminescence spectra from thermally grown oxide in thermal barrier coatings," *Materials Science and Engineering: A*, Vol. 335, No. 1-2, 2002, pp. 147–156.

[81] Tolpygo, V. K., Clarke, D., and Murphy, K., "Evaluation of interface degradation during cyclic oxidation of EB-PVD thermal barrier coatings and correlation with TGO luminescence," *Surface and Coatings Technology*, Vol. 188, 2004, pp. 62–70.

[82] Xu, Z., Wang, Z., Huang, G., Mu, R., and He, L., "Morphology, bond strength and thermal cycling behavior of (Ni, Pt) Al/YSZ EB-PVD thermal barrier coatings," *Journal of Alloys and Compounds*, Vol. 651, 2015, pp. 445–453.

[83] Peng, X. and Clarke, D. R., "Piezospectroscopic analysis of interface debonding in thermal barrier coatings," *Journal of the American Ceramic Society*, Vol. 83, No. 5, 2000, pp. 1165–1170.

[84] Jordan, E., Sohn, Y., Xie, W., Gell, M., Xie, L., Tu, F., Pattipati, K., and Willett, P., "Residual stress measurement of thermal barrier coatings using laser fluorescence technique and their life prediction," *IEEE Systems Readiness Technology Conference*, IEEE, 2001, pp. 593–603.

[85] Patel, N. V., Jordan, E. H., Sridharan, S., and Gell, M., "Cyclic furnace testing and life predictions of thermal barrier coating spallation subject to a step change in temperature or in cycle duration," *Surface and Coatings Technology*, Vol. 275, 2015, pp. 384–391.

[86] Kitazawa, R., Kakisawa, H., and Kagawa, Y., "Anisotropic TGO morphology and stress dis-

tribution in EB-PVD Y2O3-ZrO2 thermal barrier coating after in-phase thermo-mechanical test," *Surface and Coatings Technology*, Vol. 238, 2014, pp. 68–74.

[87] Sergo, V. and Clarke, D. R., "Observation of subcritical spall propagation of a thermal barrier coating," *Journal of the American Ceramic Society*, Vol. 81, No. 12, 1998, pp. 3237–42.

[88] Princeton Instruments, "LightField," 2015.

[89] The MathWorks, Inc., "MATLAB 2018a," 2018.

[90] Wang, X., Wu, R., and Atkinson, A., "Characterisation of residual stress and interface degradation in TBCs by photo-luminescence piezo-spectroscopy," *Surface and Coatings Technology*, Vol. 204, No. 15, 2010, pp. 2472–2482.

[91] Egerton, R. F., *Physical Principles of Electron Microscopy: An Introduction to TEM, SEM, and AEM*, Springer, 2005.

[92] Microscopy Australia, "Microanalysis Training Module," 2014.

[93] Zhou, L., Mukherjee, S., Huang, K., Park, Y. W., and Sohn, Y., "Failure characteristics and mechanisms of EB-PVD TBCs with Pt-modified NiAl bond coats," *Materials Science and Engineering: A*, Vol. 637, 2015, pp. 98–106.

[94] Tolpygo, V. and Clarke, D., "The effect of oxidation pre-treatment on the cyclic life of EB-PVD thermal barrier coatings with platinum–aluminide bond coats," *Surface and Coatings Technology*, Vol. 200, No. 5-6, 2005, pp. 1276–1281.

[95] Braue, W., Schulz, U., Fritscher, K., Leyens, C., and Wirth, R., "Analytical electron microscopy of the mixed zone in NiCoCrAlY-based EB-PVD thermal barrier coatings: as-coated condition versus late stages of TBC lifetime," *Materials at High Temperatures*, Vol. 22, No. 3-4, 2005, pp. 393–401.

[96] Schulz, U., Fritscher, K., and Ebach-Stahl, A., "Cyclic behavior of EB-PVD thermal barrier coating systems with modified bond coats," *Surface and Coatings Technology*, Vol. 203, No. 5-7, 2008, pp. 449–455.

[97] Kim, H. and Walter, M. E., "Characterization of the degraded microstructures of a platinum aluminide coating," *Materials Science and Engineering: A*, Vol. 360, No. 1-2, 2003, pp. 7–17.

[98] Tomimatsu, T., Zhu, S., and Kagawa, Y., "Effect of thermal exposure on stress distribution in TGO layer of EB-PVD TBC," *Acta Materialia*, Vol. 51, No. 8, 2003, pp. 2397–2405.

[99] Nychka, J., Clarke, D., Sridharan, S., Jordan, E., Gell, M., Lance, M., Chunnilall, C., Smith, I., Saunders, S., Pillan, R., et al., "NDE assessment of TBCs: an interim report of a photo-stimulated luminescence 'round-robin'test," *Surface and Coatings Technology*, Vol. 163, 2003, pp. 87–94.

[100] Witke, K., Österle, W., Skopp, A., and Woydt, M., "Raman microprobe spectroscopy and transmission electron microscopy of thermal sprayed ZrO2 coatings before and after rub testing of outer air seals," *Journal of Raman Spectroscopy*, Vol. 32, No. 12, 2001, pp. 1008–1014.

[101] Li, C. and Li, M., "UV Raman spectroscopic study on the phase transformation of ZrO2, Y2O3–ZrO2 and SO42-/ZrO2," *Journal of Raman Spectroscopy*, Vol. 33, No. 5, 2002, pp. 301–308.

[102] Lance, M., Haynes, J., Ferber, M., and Cannon, W., "Monoclinic zirconia distributions in plasma-sprayed thermal barrier coatings," *Journal of Thermal Spray Technology*, Vol. 9, No. 1, 2000, pp. 68.

[103] Ilavsky, J. and Stalick, J. K., "Phase composition and its changes during annealing of

plasma-sprayed YSZ," *Surface and Coatings Technology*, Vol. 127, No. 2-3, 2000, pp. 120–129.

[104] Chevalier, J., Gremillard, L., Virkar, A. V., and Clarke, D. R., "The tetragonal-monoclinic transformation in zirconia: lessons learned and future trends," *Journal of the American Ceramic Society*, Vol. 92, No. 9, 2009, pp. 1901–1920.

[105] Zhao, X. and Xiao, P., "Residual stresses in thermal barrier coatings measured by photoluminescence piezospectroscopy and indentation technique," *Surface and Coatings Technology*, Vol. 201, No. 3-4, 2006, pp. 1124–1131.

[106] Suzuki, K., Tanaka, K., and Shobu, T., "Residual stress in EB-PVD thermal barrier coatings," *Materials Science Forum*, Vol. 524, 2006, pp. 879–884.

[107] Zhu, J., Xie, H., Hu, Z., Chen, P., and Zhang, Q., "Cross-sectional residual stresses in thermal spray coatings measured by moiré interferometry and nanoindentation technique," *Journal of thermal spray technology*, Vol. 21, No. 5, 2012, pp. 810–817.

[108] Chen, X., Liu, Z., and Yang, Y., "Residual stress evolution regularity in thermal barrier coatings under thermal shock loading," *Theoretical and Applied Mechanics Letters*, Vol. 4, No. 2, 2014.

[109] Li, M., Sun, X., Gong, S., Zhang, Z., Guan, H., and Hu, Z., "Phase transformation and bond coat oxidation behavior of EB-PVD thermal barrier coating," *Surface and Coatings Technology*, Vol. 176, No. 2, 2004, pp. 209–214.

[110] Knipe, K., Manero II, A., Siddiqui, S. F., Meid, C., Wischek, J., Okasinski, J., Almer, J., Karlsson, A. M., Bartsch, M., and Raghavan, S., "Strain response of thermal barrier coatings captured under extreme engine environments through synchrotron X-ray diffraction," *Nature communications*, Vol. 5, 2014, pp. 4559.

[111] Knipe, K., Manero, A. C., Sofronsky, S., Okasinski, J., Almer, J., Wischek, J., Meid, C., Karlsson, A., Bartsch, M., and Raghavan, S., "Synchrotron XRD measurements mapping internal strains of thermal barrier coatings during thermal gradient mechanical fatigue loading," *Journal of Engineering for Gas Turbines and Power*, Vol. 137, No. 8, 2015, pp. 082506.

[112] Pfeiffer, C., Affeldt, E., and Göken, M., "Miniaturized bend tests on partially stabilized EB-PVD ZrO2 thermal barrier coatings," *Surface and Coatings Technology*, Vol. 205, No. 10, 2011, pp. 3245–3250.

[113] Johnson, C., Ruud, J., Bruce, R., and Wortman, D., "Relationships between residual stress, microstructure and mechanical properties of electron beam–physical vapor deposition thermal barrier coatings," *Surface and Coatings Technology*, Vol. 108, 1998, pp. 80–85.

[114] Guo, S. and Kagawa, Y., "Isothermal and cycle properties of EB-PVD yttria-partially-stabilized zirconia thermal barrier coatings at 1150 and 1300 C," *Ceramics international*, Vol. 33, No. 3, 2007, pp. 373–378.

[115] Teixeira, V., Andritschky, M., Fischer, W., Buchkremer, H., and Stöver, D., "Effects of deposition temperature and thermal cycling on residual stress state in zirconia-based thermal barrier coatings," *Surface and Coatings Technology*, Vol. 120, 1999, pp. 103–111.

[116] Zotov, N., Bartsch, M., Chernova, L., Schmidt, D., Havenith, M., and Eggeler, G., "Effects of annealing on the microstructure and the mechanical properties of EB-PVD thermal barrier coatings," *Surface and Coatings Technology*, Vol. 205, No. 2, 2010, pp. 452–464.

[117] Chirivi, L. and Nicholls, J., "Influence of Surface Finish on the Cyclic Oxidation Lifetime of an EB-PVD TBC, deposited on PtAl and Pt-diffused Bondcoats," *Oxidation of metals*, Vol. 81, No. 1-2, 2014, pp. 17–31.

[118] Gell, M., Vaidyanathan, K., Barber, B., Jordan, E., and Cheng, J., "Mechanism of spallation in platinum aluminide/electron beam physical vapor-deposited thermal barrier coatings," *Metallurgical and Materials Transactions A*, Vol. 30, No. 2, 1999, pp. 427–435.

[119] Zhang, Y., Lee, W., Haynes, J. A., Wright, I., Cooley, K., and Liaw, P., "Synthesis and cyclic oxidation behavior of a (Ni, Pt) Al coating on a desulfurized Ni-base superalloy," *Metallurgical and Materials Transactions A*, Vol. 30, No. 10, 1999, pp. 2679–2687.

[120] Zhang, Y., Knowles, D., and Withers, P., "Microstructural development in Pt-aluminide coating on CMSX-4 superalloy during TMF," *Surface and Coatings Technology*, Vol. 107, No. 1, 1998, pp. 76–83.

[121] Pint, B., Wright, I., Lee, W., Zhang, Y., Pruessner, K., and Alexander, K., "Substrate and bond coat compositions: factors affecting alumina scale adhesion," *Materials Science and Engineering: A*, Vol. 245, No. 2, 1998, pp. 201–211.

[122] Hauk, V., *Structural and Residual Stress Analysis by Nondestructive Methods*, Elsevier, 1997.